CrossMark

How Does the Thermal Environment Affect the Exosphere/Surface Interface at Mercury?

F. Leblanc[1] , M. Sarantos[2] , D. Domingue[3] , A. Milillo[4] , D. W. Savin[5] , P. Prem[6] , J. Benkhoff[7], J. Zender[7], A. Galli[8] ,
G. Murakami[9], S. Sasaki[10], M. Thompson[11], and J. Raines[12]

[1] LATMOS/CNRS, Sorbonne University, Paris, France; francois.leblanc@latmos.ipsl.fr
[2] NASA Goddard Space Flight Center, Greenbelt, MD, USA
[3] Planetary Science Institute, Tucson, AZ, USA
[4] INAF/Istituto di Astrofisica e Planetologia Spaziale, Roma, Italy
[5] Astrophysics Laboratory, Columbia University, New York, NY, USA
[6] Johns Hopkins Applied Physics Laboratory, Laurel, MD, USA
[7] ESA, ESTEC, Netherlands
[8] Planetary Sciences Division, University of Bern, Switzerland
[9] ISAS, JAXA, Japan
[10] Department of Earth and Space Science, Osaka University, Japan
[11] Purdue University, West Lafayette, IN, USA
[12] Climate and Space Sciences and Engineering, University of Michigan, Ann Arbor, MI, USA

Abstract

The fate of Mercury's exospheric volatiles and, in a lesser way, of the refractory particles absorbed in the first few centimeters of the surface both depend highly on the temperature profile with depth and its diurnal variation. In this paper, we review several mechanisms by which the surface temperature might control the surface/exosphere interface. The day/night cycle of the surface temperature and its orbital variation, the temperature in the permanent shadow regions, and the subsurface temperature profiles are key thermal properties that control the fate of the exospheric volatiles through the volatile ejection mechanisms, the thermal accommodation, and the subsurface diffusion. Such properties depend on the solar illumination from large to small scales but also on the regolith structure. The regolith is also space-weathered by the thermal forcing and by the thermal-mechanical processing. Its composition is changed by the thermal conditions. We conclude by discussing key characteristics that need to be investigated theoretically and/or in the laboratory: the dependency of the surface spectra with respect to temperature, the typical diffusion timescale of the volatile species, and the thermal dependency of their ejection mechanisms.

1. Introduction

With a solar photon flux 1 order of magnitude larger than at the Earth, Mercury's radiative environment is a strong driver of space weathering. The solar flux controls the quantity, depth, and state of the exospheric particles penetrating the first tens of centimeters of the upper surface and is one of the main drivers of the spatial and temporal variabilities in the exosphere.

Due to its high eccentricity, the solar flux at Mercury varies by more than a factor of 2 between perihelion and aphelion, leading to Mercury's subsolar surface temperature varying from ∼700 to ∼100 K (Morrison 1970; Chase et al. 1976). Moreover, Mercury's 3:2 spin–orbit resonance (Colombo & Shapiro 1966; Soter & Ulrichs 1967) leads to the concept of hot and warm longitudes. Hot longitudes are specific regions facing the Sun at perihelion that, during the 2 Mercury yr diurnal cycle (that is, 176 Earth days), receive an average of 2.6 times more photons than the warm longitudes, which are facing the Sun at aphelion (Langevin 1997).

On the other hand, Mercury's small obliquity allows the existence of permanently shadowed areas (Harmon & Slade 1992; Slade et al. 1992) in high-latitude craters that could harbor water ice and are stable on geological timescales (Paige et al. 1992). The fate of the exospheric volatiles and, in a lesser way, of the refractory particles absorbed in the first centimeters of the surface highly depends on the temperature profile with depth and its diurnal variation, which is controlled not only by the diurnal cycle but also by the local thermal conductivity and grain size (Vasavada et al. 1999; Hale & Hapke 2002).

Solar photons, together with ions, electrons (Raines et al. 2023), and micrometeoroids (Krueger et al. 2023), are an important factor in the release of weakly bound species from the surface, such as volatiles (Wurz et al. 2022, 2023). Volatiles have also been observed by the NASA MErcury Surface, Space ENvironment, GEochemistry and Ranging (MESSENGER) mission, which performed several years of exospheric observations around Mercury (Cassidy et al. 2016; Vervack et al. 2016). Several mechanisms of ejection of these volatiles from the surface have been described and reproduced in the laboratory (Milillo et al. 2023). The efficiency of these mechanisms (in particular, photon-stimulated desorption, PSD, and thermal desorption) is species-dependent but also depends on the surface characteristics (Wurz et al. 2023) and the surface temperature.

This review paper is one of the products from the workshop "Mercury's Surface Response to the Interplanetary Environment:

Identifying Needed Studies in Laboratory Astrophysics." During that workshop, several questions were discussed and debated, among which was the question regarding the role of the thermal conditions at Mercury in the formation and evolution of the exosphere. This paper provides an overview of that discussion and open questions that need to be addressed to further progress in our understanding of the relationship between the surface and exosphere at Mercury. More specifically, here, we cover the topic "How does the radiative environment affect the lifetime of volatile and refractory elements on the surface of Mercury?" The other three reviews cover complementary topics and can be found in this Focus Issue (Wurz et al., Krüger et al., and Raines et al.).

In this paper, we focus on the various signatures of solar radiative forcing on the thermal state of the surface by discussing the diurnal cycle of the surface temperature (Section 2.1), the existence of specific regions at the top surface (Section 2.2), and the typical temperature profile of the first meter below the surface. In Section 3, we discuss the effects of three particular properties of the surface that control the temperature: the solar illumination (Section 3.1), the regolith physical structure (Section 3.2), and the particulate properties (Section 3.3). Section 4 describes the links between the surface temperature and the exosphere, how the various ejection mechanisms depend on the surface temperature (Section 4.1), how temperature also controls the diurnal exospheric cycle (Section 4.2), and the apparent relationship between warm longitude and the sodium exospheric spatial distribution (Section 4.3). Section 5 is devoted to describing the changes induced in the top surface by the thermal forcing: the thermal space weathering (Section 5.1), the spectral signatures (Section 5.2), and the surface composition (Section 5.3). Based on our present knowledge of the relationship between thermal radiative forcing and the surface and exosphere interconnections, we then discuss in Section 6 what appear to be the key measurements needed to further improve this knowledge; specifically, the dependency of the spectral signatures of the surface with respect to temperature (Section 6.1), the typical diffusion timescale in the top layer of the regolith of the exospheric species (Section 6.2), and the dependencies of the various ejection mechanisms from the surface into the exosphere with respect to the surface temperature (Section 6.3). We conclude this paper in Section 7.

2. Thermal Properties of Mercury's Surface

The primary mechanisms controlling the surface temperature are solar irradiation, radiative loss, and thermal conduction (Cuzzi 1974; Ledlow et al. 1992; Mitchell & De Pater 1994; Vasavada et al. 1999; Hale & Hapke 2002; Yan et al. 2006; Bauch et al. 2021). Scattered insolation and infrared (IR) emission from surrounding areas might also be important in specific areas like permanently shadowed craters (Vasavada et al. 1999; Paige et al. 2013). The regolith thermophysical properties (density, thermal conductivity, heat capacity, etc.) also control the evolution of the temperature along a diurnal cycle, as well as the thermal diffusion through the regolith (Section 3).

2.1. Diurnal Cycle

Mercury's subsolar surface temperature varies from ∼700 K (Morrison 1970) to ∼100 K (Chase et al. 1976). Figure 1

displays the surface temperature evolution along one diurnal cycle at four positions on the surface of Mercury as calculated by Bauch et al. (2021). Those authors used a one-dimensional heat conduction model in a semi-infinite medium, similar to many previous authors (Soter & Ulrichs 1967; Morrison 1970; Chase et al. 1976; Henderson & Jakosky 1997; Vasavada et al. 1999),

$$\rho(z)C(T)\frac{\partial T(z,t)}{\partial t} = \frac{\partial}{\partial z}\left(k(z,T)\frac{\partial T(z,t)}{\partial z}\right),\qquad(1)$$

where ρ is the density, C is the heat capacity, T is the temperature, t is the time, z is the depth, and k is the thermal conductivity. The upper boundary condition is set by the following equation:

$$\varepsilon\sigma T^4(z=0,t) = F(t) + \left[\frac{\partial T(z,t)}{\partial z}\right]_{z=0},\qquad(2)$$

where ϵ is the emissivity of the surface, σ is the Stefan–Boltzmann constant, and F is the solar insolation, given by

$$F(t) = \frac{S_0}{(R(t))^2}\cos(\theta(t))\times(1-A),\qquad(3)$$

which depends on the surface albedo A, the distance R of Mercury from the Sun, and the solar incidence angle θ (Bauch et al. 2021). S_0 is the solar flux at 1 au, equal to 1367 W m^{-2}. The lower boundary of Equation (1) is constrained by a geothermal flux that has a limited effect on the derived surface temperature (Vasavada et al. 1999).

Thermal conductivity is usually described as the sum of two terms—a radiative term that is strongly temperature-dependent and a solid conduction term (within and between grains). The relative importance of these two terms varies with depth as the porosity decreases (Ledlow et al. 1992; Mitchell & De Pater 1994). The thermal conductivity is given by

$$k(z,T) = k_c(z)\left[1 + \chi(z)\left(\frac{T(z)}{T_{350}}\right)^3\right],\qquad(4)$$

where k_c represents the contact conductivity, and $T_{350} = 350$ K. The first term in this equation corresponds to the solid conductivity, and χ is the ratio between the radiative and solid conductivity. Vasavada et al. (1999) have shown the effect of these two terms on the mean subsurface temperature. When the radiative term is small with respect to the solid conduction term, the heat conductivity is similar on the day- and nightsides, leading to a mean subsurface temperature that is constant with depth. But when the radiative term is nonnegligible, even in the first few centimeters of the layer, the thermal energy is conducted more efficiently downward during the day than upward during the night, leading to a hotter mean subsurface temperature at a few tens of centimeters compared to the case dominated by solid conduction.

As pointed out by Hale & Hapke (2002), an explicit assumption of Equation (4) is the radiative equilibrium of the regolith. Hapke (1996) underlined that Equation (4) is a good approximation deep in the regolith but not near the surface, where radiation escapes to space and is not in equilibrium with the medium. In this situation, radiative transfer within the medium can no longer be modeled accurately by the T^3 term in Equation (4) but can instead be modeled by solving the
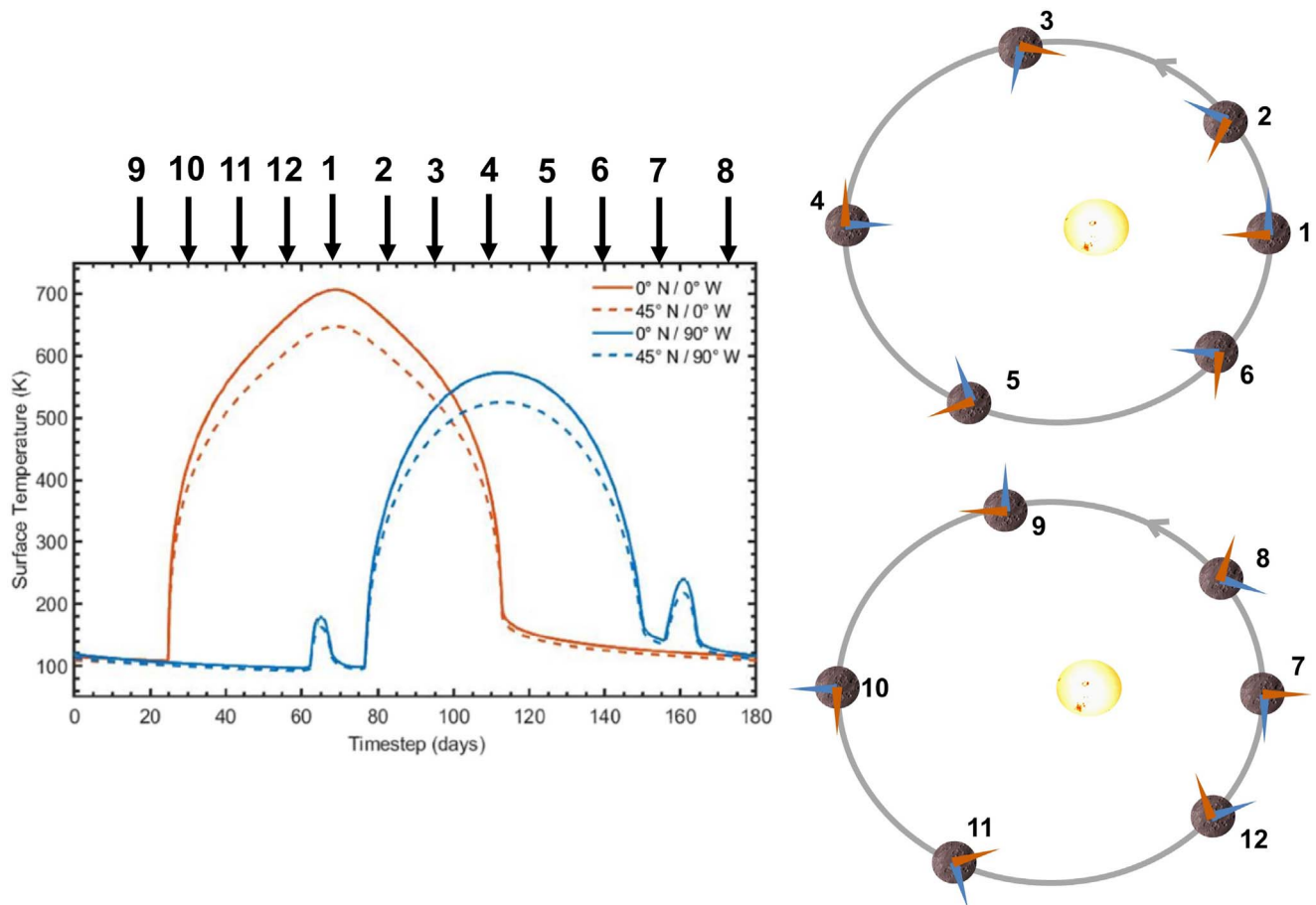
Figure 1. Left panel: diurnal cycle of the surface temperatures at two latitudes, dotted lines at 45° north and solid lines at 0°, and two longitudes in orange at 0° west longitude and blue at 90° west longitude (from Bauch et al. 2021). The arrows with numbers at the top of the left panel correspond to the approximate respective positions displayed in the right panel. Right panel: position of the 0° west longitude in orange and the 90° west longitude in blue in the orbital plane of Mercury around the Sun during the first year (top panel for positions numbered 1–6) and during the second year (bottom panel for positions numbered 7–12; adapted from Langevin 1997). The gray ellipse represents the orbit of Mercury around the Sun as seen from the north.

radiative transfer equation, as in Henderson & Jakosky (1994, 1997), Hale & Hapke (2002), and Wohlfarth et al. (2023). The main consequences of accounting for radiative nonequilibrium are as follows, according to Hale & Hapke (2002).

1. A slightly lower maximum daytime surface temperature, because the classical radiative equilibrium model makes the assumption that all of the solar radiation is deposited at the surface and all thermal emission to space originates from the surface.
2. A steeper decrease in temperature after sunset and a steeper increase after sunrise in the radiative nonequilibrium model, because lower temperatures imply a lower radiative contribution to conductivity (see Equation (4)).

In Figure 1, the dashed and solid lines of the same color show the dependency of the temperature with latitude, whereas the two sets of lines of different colors correspond to two different planetary longitudes. An albedo of 0.05 was used for this calculation (Bauch et al. 2021). For longitude 0°W (solid orange line in Figure 1), local noon occurs at perihelion, whereas for longitude 90°W, it occurs at aphelion (solid blue line in Figure 1). Because of Mercury's high eccentricity (with a heliocentric distance varying from 0.31 au at perihelion to 0.47 au at aphelion), the solar insolation $F(t)$ varies by a factor

of ~2 (Morrison 1970). As a consequence, the maximum surface temperature varies from 706 K at perihelion (solid orange line) to 573 K at aphelion (solid blue line), as displayed in Figure 1. Moreover, due to the ratio of Mercury's angular velocity with respect to the spin rate, there is an apparent retrograde solar motion around perihelion leading to two sunsets and sunrises associated with the secondary peaks apparent at longitude 90°W, as shown in Figure 1 (solid and dashed blue lines). The third peak of the surface temperature of the blue lines in Figure 1 at a time of 160 Earth days is 40 K larger than the first peak at a time of 70 Earth days because of the heat stored in the subsurface during the dayside.

The daytime surface temperature is largely dominated by the solar insolation (Equation (2)) and the subsurface thermophysical properties on the nightside (Equation (1)). As shown by Morrison (1970), the decrease of the surface temperature on the nightside is controlled by the thermal inertia $\sqrt{k\rho C}$ (also calculated using $\sqrt{k_c \rho C}$). To fully characterize the regolith, Hale & Hapke (2002) also introduced the conductivity ratio $k_c E_T$, where E_T is the extinction coefficient that characterizes the capability of thermal radiation to travel through the regolith before being absorbed or scattered (this is inversely related to the radiative conductivity). The quantity $k_c E_T$ is similar to $1/\chi$ in Equation (4).
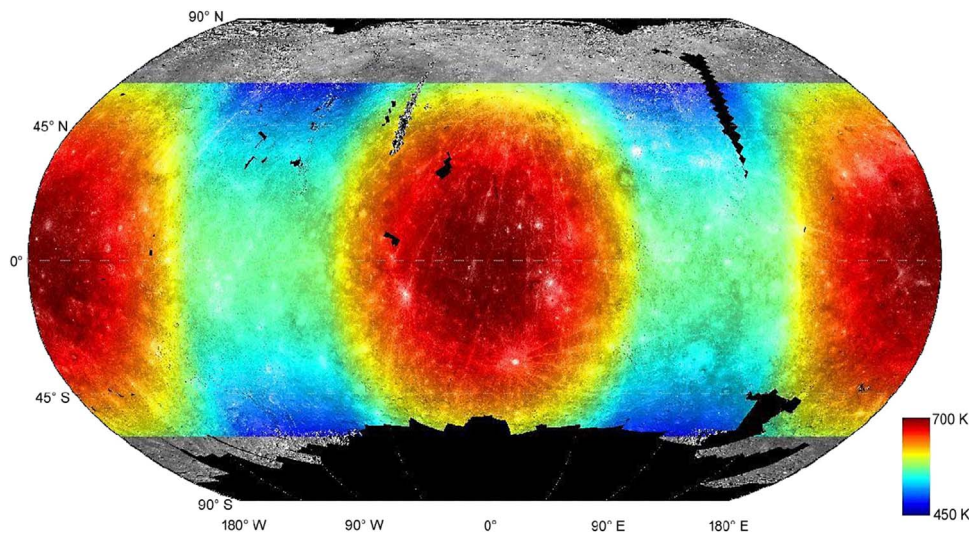
Figure 2. Map of the modeled local maximum surface temperatures superposed on MESSENGER MDIS surface albedo map (Bauch et al. 2021). Bauch et al. (2021) excluded the polar regions from their analysis due to a lack of usable albedo data.

Mercury's 3:2 spin–orbit resonance (Colombo & Shapiro 1966; Soter & Ulrichs 1967) leads to the concept of hot and warm longitudes. The hot longitude corresponds to the 0°W and 180°W longitudes, which are at noon local time at perihelion. The 0°W longitude is indicated with an orange triangle in the right panel of Figure 1, and its surface temperature is shown by a solid orange line in the left panel of Figure 1. The 180°W longitude follows the same evolution. Such hot longitudes receive an average of 2.6 times more photons than the warm longitudes, at 90°W and 270°W, over the 2 yr diurnal cycle (that is, 176 Earth days; Langevin 1997). Longitude 90°W is illustrated in the right panel of Figure 1 by the blue triangle, and its subsolar temperature is displayed in the left panel of Figure 1 with a blue solid line. As a consequence of the 3:2 spin–orbit resonance, the maximum equatorial temperatures at longitudes 0°W and 180°W (hot poles) are about 130 K higher than at longitudes 90°W and 270°W (warm poles). Figure 2 displays the maximum surface temperature as calculated by Bauch et al. (2021) using a model based on Equations (1)–(3).

2.2. Polar Regions: Permanently Shadowed Regions

Mercury's small obliquity allows for permanently shadowed regions (PSRs) in high-latitude craters (Chabot et al. 2013). Earth-based radar images of Mercury (Harmon & Slade 1992; Slade et al. 1992) strongly suggested the presence of water-ice deposits that were determined to reside within PSRs and remain stable over geologic timescales (Paige et al. 1992). Harmon et al. (2011) compiled 6 yr of Arecibo radar observations and concluded that ice is stable in PSRs, but that some of these relatively pure ice deposits are covered by a thin layer of insulating dust as suggested by theoretical modeling (Vasavada et al. 1999). Harmon et al. (2011) also showed that the low-latitude ice appears to be modulated in longitude by the hot longitude effect, as illustrated in Figure 2. This conclusion was confirmed by Chabot et al. (2013) using Mercury Dual Imaging System (MDIS) Wide Angle Camera (WAC) observations from MESSENGER. Paige et al. (2013) used detailed Mercury Laser Altimeter (MESSENGER/MLA) topography maps of the northern hemisphere to develop a detailed model of the biannual maximum temperature (Figure 3). These authors

demonstrated a relation between apparent bright radar terrain and a biannual average temperature of less than 100 K and no radar-bright deposits in regions where the biannual average temperature was higher than 100 K. These findings strongly suggested that the radar-bright deposits are water ice. Indeed, temperatures between 100 and 115 K correspond to a 1 mm Gyr^{-1} rate of sublimation of exposed water ice or water ice buried beneath a 10 cm thick lag deposit (see also Gläser & Oberst 2023; Glantzberg et al. 2023). The sublimation temperature of other potential candidates for this radar-bright material, such as SO_2 or S (Sprague et al. 1995), do not fit with the apparent relation between the radar-bright deposit and the less than 100 K biannual temperature (Paige et al. 2013). This conclusion was also confirmed by MESSENGER's Neutron Spectrometer (NS), which measured a decrease in the flux of epithermal and fast neutrons in the north polar region consistent with the presence of long-standing water ice (Lawrence et al. 2013). Based on the NS measurements, Lawrence et al. (2013) also concluded that Mercury's radar-bright deposits contain a hydrogen-rich layer more than tens of centimeters thick beneath a depleted layer of 10–30 cm thickness. This conclusion was also confirmed by Neumann et al. (2013) using MLA reflectance measurement inside Prokofiev crater (a 112 km diameter crater at ∼85.8°N and 62.9°E).

Deutsch et al. (2016) combined MESSENGER MDIS WAC images and MLA altimetric measurements to map the shadowed areas of the north polar region and concluded that between 13% and 17% of the surface between 85°N and 90°N is in persistent or permanent shadow, a percentage that decreases to 3.7% and 4.1% between 80°N and 90°N. This mapping of the north polar regions also highlighted a significant portion that did not correspond to radar-bright areas measured from Earth-based radar, suggesting either some limitation due to the viewing geometry of the radar or a variability in the deposits in these shadow areas that needs to be further investigated. Rivera-Valentín et al. (2022) recently identified a gradation in the radar-scattering properties of Mercury's north polar deposits that may be attributable to variations in ice purity.

Considering that these radar-bright features are associated with relatively pure ice covered by at most a thin layer of lag
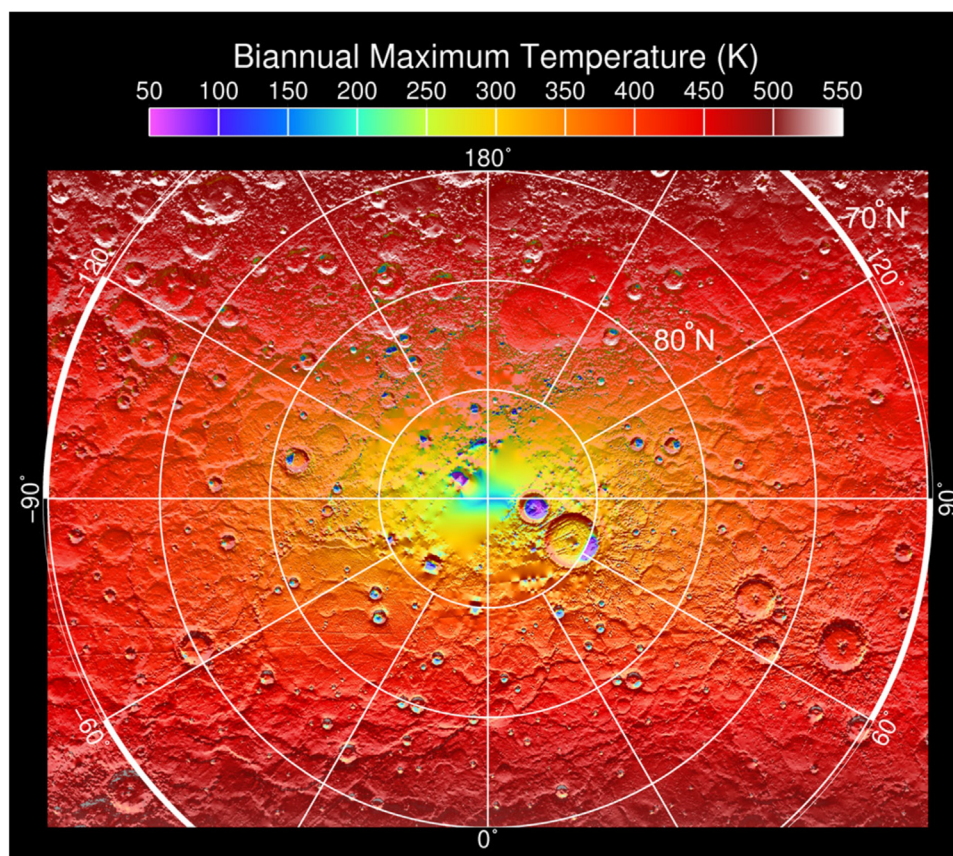
Figure 3. Calculated maximum temperature in the north polar region of Mercury superposed on a shaded relief map of MESSENGER-derived topography (from Paige et al. 2013).

material, Paige et al. (2013) suggested a geologically recent origin for this water ice. Photodissociation by Lyα would limit its stability on longer timescales (Morgan & Shemansky 1991). By analyzing the distribution of the MLA-dark material above 84°N, which is present in regions with a biannual average temperature of 100 K and absent in regions with temperatures higher than 210 K, Paige et al. (2013) suggested that water-ice sublimation is the origin of the distribution of this dark material. A more extended distribution of the water ice may have occurred in the past, with the water then having sublimated and migrated toward the more thermally stable area (the radar-bright region), leaving sublimation lags corresponding to the dark area, which may be the remaining parts of asteroidal or cometary materials. In another way, the origin of the water-ice deposits suggested by the correlation between the radar-bright signatures and the less than 100 K biannual temperature would be of asteroidal or cometary origins (Jones et al. 2020; Schörghofer et al. 2021) and formed by the migration of water into these areas from the original impact sites (Ernst et al. 2018).

Developing one of the first full thermal models of a crater (described as a bowl-shaped surface), Vasavada et al. (1999) studied the effects of the insolation cycle, crater shapes, multiple scattering of sunlight and IR radiation, and temperature-dependent regolith thermophysical properties on the temperatures of PSRs. These authors demonstrated that the crater shape is more important than its latitudinal position. Indeed, the inclination of the walls of deep craters controls the incidence angle of the sunlight but also the scattering and emission of heat toward the interiors of these craters.

Topography also appears important at small scales. The absence of exospheric heat transport and the surface roughness might lead to large temperature variability at small scales (Hayne & Aharonson 2015). Rubanenko et al. (2018) have modeled the influence of small-scale topography and shadowing on the thermal stability of volatiles on Mercury. Prem et al. (2018) investigated the influence of small-scale temperature variations on volatile transport and found that this could influence the cold-trapping properties of the lunar poles, as well as the exospheric structure near dawn. These same effects would be active on Mercury.

2.3. Temperature: Upper Surface Profile

As summarized by Vasavada et al. (1999), decades of observations of Mercury and the Moon's surface have led to several conclusions on their properties:

1. the Moon and Mercury near-surface layers are structurally similar,
2. the density increases with depth (Winter & Saari 1969), and
3. the rapid cooling of the uppermost layer just after sunset and its slow cooling during the night implies a rapid change with depth of the thermophysical properties of the surface. Such a structure, with a few centimeters of insulating thermal layer atop a highly compacted layer, has been explained by the effect of micrometeorite bombardment (Mitchell & De Pater 1994).
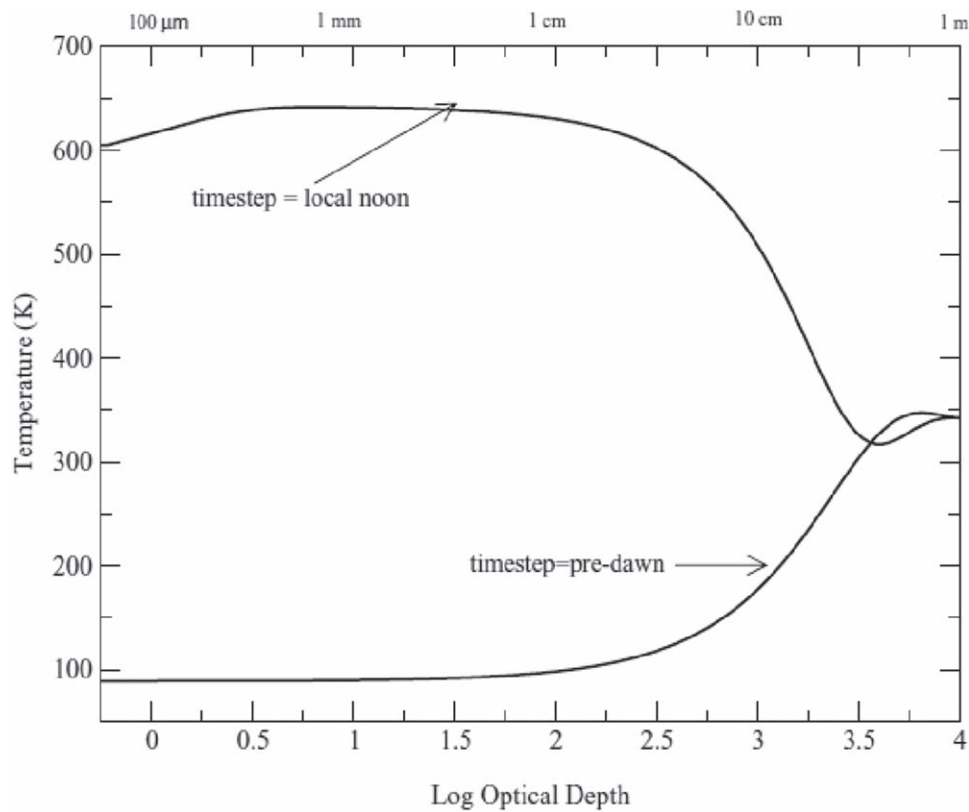
Figure 4. Thermal profile with depth as calculated by Hale & Hapke (2002) for a single-layer model and for a thermal inertia of 67 J m^{-2} s$^{-1/2}$ K^{-1} and a conductivity ratio of 50 J m^{-2} s^{-1} K^{-1}.

Hale & Hapke (2002) also modeled the effect of the diurnal cycle on the thermal profile. During the day, the solar heat is transferred to deeper layers because of the generally high near-surface temperatures, leading to an efficient radiative conductivity. During the night, radiative conductivity is significantly decreased because of the low temperature of the top layers of the surface. Heat is therefore trapped below the surface. Figure 4 displays the temperature profile for a set of thermal inertia and conductivity ratios, leading to a very good fitting of the Mariner 10 Infrared Radiometer (IRR) observations on the nightside of Mercury (Chase et al. 1976; Bandfield et al. 2019). As shown in this figure, this heat wave penetrates up to a few tens of cm inside the regolith and peaks in temperature a few hundred μm below the surface, due to the radiation penetration depth in the regolith.

A profile as displayed in Figure 4 is crucial to follow the fate of the exospheric volatiles and, in a lesser way, the refractory particles absorbed in the top centimeters of the surface, which highly depends on the temperature profile with depth (Reiss 2018) and its diurnal variation.

3. Controls on the Regolith Temperature

The controls on the regolith temperature can be grouped into three categories, each influencing the other. These are the incident solar illumination, the physical structure of the regolith, and the particulate properties. Solar illumination is the primary heat source, varies as a function of longitude and latitude due to Mercury's spin–orbit resonance, and is modulated by the surface roughness at both large and small scales. The large-scale roughness, or surface topography, is the roughness at or above the detector limit (instrument footprint

spatial resolution) and creates shadowed regions, some permanently near the poles (e.g., Vasavada et al. 1999; Paige et al. 2013; Bauch et al. 2021). Small-scale roughness is the roughness below the detector limit (instrument footprint spatial resolution, i.e., subpixel scale for an imager) and also creates shadows that modulate mean surface temperatures (e.g., Bandfield et al. 2015). The physical structure of the regolith includes particle size and size distribution, porosity, and density, each of which varies as a function of depth (e.g., Reiss 2018; Ryan et al. 2020; Rognini et al. 2022; Ryan et al. 2022). In addition, the thermal properties of the regolith particles, whether they behave isothermally or nonisothermally, also play a role in the regolith's overall temperature structure with depth (Ryan et al. 2022).

3.1. Solar Illumination

Bauch et al. (2021) calculated surface temperatures (Figure 2) assuming lunar-like thermal properties and that these properties are uniform across Mercury's surface using surface albedo and topography based on MESSENGER MDIS observations (Hawkins et al. 2007; Becker et al. 2016). Examination of the Mariner 10 IRR nightside observations supports the assumption that the thermal properties are mostly uniform across Mercury's surface, with exceptions correlated to notable geologic units (Bandfield et al. 2019). Bandfield et al. (2019) converted the observed IRR brightness temperature to surface kinetic temperature using lunar emission angle-dependent emissivity derived from lunar Diviner data and thus also assuming lunar-like thermal properties for Mercury's surface.

Small-scale surface roughness (subpixel roughness) affects both the stability and transport of volatiles (Prem et al. 2018; Rubanenko et al. 2018; Davidsson & Hosseini 2021). Volatile stability is impacted by the effects on the sublimation rate or the average residence time (time on the surface between ballistic hops), and volatile transport is affected by changes in the velocity distribution of molecules as they leave the surface. The source of these influences on stability and transport is, in part, due to the variations in surface temperature at the subpixel level (subpixel temperatures). Subpixel roughness creates localized temperature variations via self-shadowing (the Sun is below the local horizon) and mutual shadowing (obstruction of sunlight from nearby surfaces) that affect the average residence time and velocity distribution of molecules as they leave the surface. These in turn affect the rate at which molecules can migrate to cold traps, which are shaded regions on the surface where temperatures are sufficiently low such that volatiles are stable for a period of time. The rate of molecule migration in turn affects the susceptibility to photodissociation by impacting the time spent in the exosphere (Prem et al. 2018). This also influences exospheric structures, such as scale height and terminator characteristics, and the ability of cold traps to provide reservoirs of volatiles within the surface.

Small-scale roughness affects the sticking probabilities due to differences in either subpixel temperature distributions and/or desorption activation energies that affect the residence time. Different volatile species will have different desorption energies; thus, the effects of small-scale roughness will vary with volatile species.

The residence time (t_{res}) is proportional to $e^{E_a/k_B T}$, with E_a the desorption activation energy and k_B the Boltzmann constant, whereas the mean thermal velocity ($\bar{\nu}$) is proportional to $\sqrt{T}$; thus, the influence on the velocity of migrating molecules, as well as the exospheric scale height, is relatively smaller (Prem et al. 2018). Monte Carlo simulations of the effects of subpixel temperature variations due to self- and mutual shadowing show that these shadowed regions provide temporary trapping or shelter to migrating molecules, thereby slowing the rate of migration across the surface (Prem et al. 2018).

At higher latitudes and near the terminator (higher solar incidence angles), the increased amount of shadow and colder subpixel temperatures create regions that can concentrate migrating molecules, leading to a preferential depletion of the exosphere via cold trapping (Prem et al. 2018). However, the distribution of temperatures over a subpixel rough surface also increases the amount of thermal escape, which can be additionally enhanced on a surface with large temperature gradients (Prem et al. 2018), such as that on Mercury. The effects of subpixel surface roughness on lunar simulations show an ∼4%–7% increase in cold-trap capture between a smooth surface and a subpixel rough surface (Prem et al. 2018). Including the effects of subpixel surface roughness also results in a reduced and broadened peak in normalized column density at the dawn terminator of the exosphere, especially at equatorial latitudes (Prem et al. 2018). Exospheric density is greater at higher latitudes, and this is also enhanced when subpixel surface roughness is included in the modeling (Prem et al. 2018). While similar exospheric simulations have not yet been performed for Mercury, the effect of surface roughness is likely to be qualitatively similar, since the Moon and Mercury are thought to have similar thermophysical properties (e.g.,

Vasavada et al. 1999). Examination of the formation of "micro cold traps" on the lunar surface on 1 km to 1 cm scales shows that in the lunar case, ∼10%–20% of the polar cold traps are in these micro cold traps and that they extend the polar cold-trapping region down to 80° latitude (Hayne et al. 2021). For Mercury, Rubanenko et al. (2018) find that cold traps in the 1–10 m scale may occupy 1%–2% of Mercury's polar regions; smaller, sub-1 m regions of shadow may exist but are less likely to be effective cold traps due to generally higher temperatures on Mercury.

3.2. Regolith Physical Structure

The thermal conductivity is influenced by composition, particle size, porosity, and temperature.

Heat transfer within Mercury's regolith will be dominated by radiation between particles and conduction through the particles at their contact points (Wesselink 1948; Watson 1964; Wechsler et al. 1972; van Antwerpen et al. 2010; De Beer et al. 2018; Ryan et al. 2020). The majority of the work thus far has focused on the radiative component. Thermal conductivity from conduction through contact points (solid conductivity) is typically much smaller than the thermal conductivity of the particles themselves (material conductivity) and is severely limited by the very small amounts of contact between particles (Ryan et al. 2020). Whereas radiative conductivity increases linearly with particle diameter, solid conductivity only changes modestly (Ryan et al. 2020).

There are numerous approaches to modeling thermal conductivity in powdered media (e.g., Gundlach & Blum 2012; Sakatani et al. 2017; Wood 2020; Ryan et al. 2022). For example, Sakatani et al. (2017) approximates the void spaces in powdered media using one-dimensional thermal radiation between multiple infinitely thin parallel planes. Wood (2020) uses analytic and mechanistic models to calculate effective thermal conductivity based on Maxwell–Eucken theoretical expressions for both the upper and lower bounds in a heterogeneous, isotropic material. Here we present the approach of Ryan et al. (2022) as an example that examines the role of particle size distributions. Modeling studies of the effects of particle size distribution, mono- versus polydisperse size distributions, show that the radiative thermal conductivities (radiative conductivity) of regolith with a mixture of particles with different sizes are identical to a monodisperse regolith with an effective size similar to the Sauter mean (surface area–weighted mean particle size; Ryan et al. 2020). However, the particle size ranges examined in the Ryan et al. (2020) study may have been too narrow to conclusively distinguish between the Sauter mean and the volumetric median (Ryan et al. 2022).

Radiative heat transfer is determined from the temperature, emissivity, and distance between radiating surfaces. Two contributions to the radiative conductivity are described by van Antwerpen et al. (2012): short-range radiation that comes from immediately adjacent particles and long-range radiation from nonadjacent particles that are within a line of sight (Ryan et al. 2020). The thermal conductivity of the particle material influences both components of the radiative thermal conductivity (Breitbach & Barthels 1980; Singh & Kaviany 1994; van Antwerpen et al. 2012; Ryan et al. 2020), such that thermal gradients within the particles themselves, their nonisothermality, would lower the rate of change in radiative thermal conductivity with temperature (Ryan et al. 2020).

Ryan et al. (2022) derived an updated expression for radiative conductivity (k_r) that accounts for porosity, particle size, and the nonisothermality of the particulates, which is given by

$$k_r = 4\sigma F(\varepsilon, \phi) f_k(k_m(T), D, T) D \overline{T}^3, \quad (5)$$

where D is the particle diameter (or Sauter mean particle diameter in the polydisperse case), T is the temperature (with mean temperature given by $\overline{T}$), F is the radiative exchange factor, f_k is the correction factor for particle nonisothermality, and σ is the Stefan–Boltzmann constant. Wu et al. (2020) provide a formulation for F that explicitly focuses on the contribution from porosity and is given by

$$F = \varepsilon \left[a + b \left(\frac{\phi}{1 - \phi} \right)^c \right], \quad (6)$$

where ϵ is the emissivity, ϕ is the porosity, and $a = 0.8049$, $b = 0.3728$, and $c = 1.6214$. The correction factor for particle nonisothermality is provided by

$$f_k = a_1 \tan^{-1} \left(a_2 \left(\frac{1 - \phi}{\Lambda_s} \right)^{a_3} \right) + a_4, \quad (7)$$

where $a_1 = -0.500$, $a_2 = 1.351$, $a_3 = 0.741$, $a_4 = 1.007$, and Λ_s is given by

$$\Lambda_s = \frac{k_m}{4 D \sigma T^3}, \quad (8)$$

where k_m is the solid conductivity (Ryan et al. 2022). Ryan et al. (2022) show that the thermal inertia of coarse regolith (>5 mm) is largely independent of regolith porosity, except where the particles themselves have significant thermal gradients. Such deviations from isothermality can be caused by a combination of large particle size, low k_m, and high mean temperatures. Assuming a lunar-like particle size distribution and the high temperatures (Figure 2), the particles on Mercury have the potential to be highly nonisothermal, and porosity will be important in the radiative conductivity of the surface.

3.3. Particulate Properties

The properties of the grains that comprise the regolith, as described in the previous section, can influence the radiative thermal conductivity of the surface. While the thermal conductivity of isothermal grains strongly depends on the porosity or grain size (Ryan et al. 2020, 2022), nonisothermal grains will induce a dependency of the thermal conductivity from the regolith structure (Ryan et al. 2020, 2022). Particles of larger size (e.g., a few millimeters to centimeters) with low material conductivity (k_m) and environments of high temperature contribute to particle nonisothermality (Ryan et al. 2020, 2022).

The high agglutinate content of the lunar regolith is considered responsible for the significantly low thermal conductivity of the solid particles, while the small grain size and porosity contribute to the low thermal conductivity of the bulk regolith. Agglutinates are the glass-welded conglomerate of particles formed primarily though micrometeoroid impact, and the volume percent of agglutinates within Mercury's regolith will be much higher than that in the lunar regolith (e.g., Cintala 1992; Domingue et al. 2014).

Simulations by Ryan et al. (2020) show that radiative thermal conductivity scales with the cube of the temperature when k_m is high (>1 W m^{-1} K^{-1}); however, lower values of k_m cause the radiative thermal conductivity to decrease, especially for higher temperatures. For extreme cases, such as a k_m of 0.05 W m^{-1} K^{-1} or lower, the radiative conductivity scaled linearly with temperature (Ryan et al. 2020). Mercury's regolith, with its high agglutinate content, falls in the latter category for lower thermal conductivities.

4. Surface Temperature and Exospheric Content

The surface temperature influences the resulting exospheric gas densities inside the regolith via (1) a dependence of (some of the proposed) source rates on temperature, (2) a dependence on temperature and temperature gradients with depth of subsurface transport properties, and (3) storage of previously released atoms and molecules. The complex interplay between instantaneous and previously released atoms and molecules gives rise to diurnal and seasonal cycles for exospheric constituents.

4.1. Dependency on the Ejection Mechanisms with Respect to Temperature

Several of the proposed sources for Mercury's exosphere (thermal desorption, electron-stimulated desorption (ESD), PSD, chemical sputtering, particle sputtering, and micrometeoroid impact vaporization; see Wurz et al. 2022 for further details) depend on temperature. Thermal desorption refers to the thermal release of bound material from the interior of a grain, as well as the release of previously deposited material on the surface of grains. Atoms and molecules may overcome the potential barrier to desorption, or bond to the surface, via thermal random motion. Desorption from the grain interior is limited by the volume diffusion rate (Killen et al. 2004). The exponential dependence of the residence time of adsorbates on substrate temperature leads many surface-gas systems to freeze gas on the nightside surface and rapidly release the gas when the surface warms near dawn (e.g., see review by Grava et al. 2021). The fact that the regolith is not isothermal further complicates the residence time calculation. Davidsson & Hosseini (2021) have demonstrated how surface roughness (due to its effects on the surface's isothermal properties) significantly increases the retention of volatiles until much later local times.

PSD and ESD also depend on surface temperature. A temperature-dependent PSD cross section for neutral sodium emission was experimentally determined for sodium adsorbates (Yakshinskiy & Madey 2004). In the case of a powderlike regolith, additional dependence on the effective PSD rate can be imparted by a temperature-dependent sticking coefficient, which results in the competition between desorption and diffusion within the top 1 mm of regolith. Due to these competing effects, it is possible that the effective PSD rate from the regolith does not monotonically increase or decrease with temperature, depending on the mobility of sodium adsorbates (Sarantos & Tsavachidis 2020). It has also been proposed that the velocity distribution of atoms from PSD is temperature-dependent (Gamborino & Wurz 2018), although the experiments cited as evidence were not performed on the same substrate. Similarly, the cross section of ion emission from ESD depends upon substrate temperature. McLain et al. (2011)
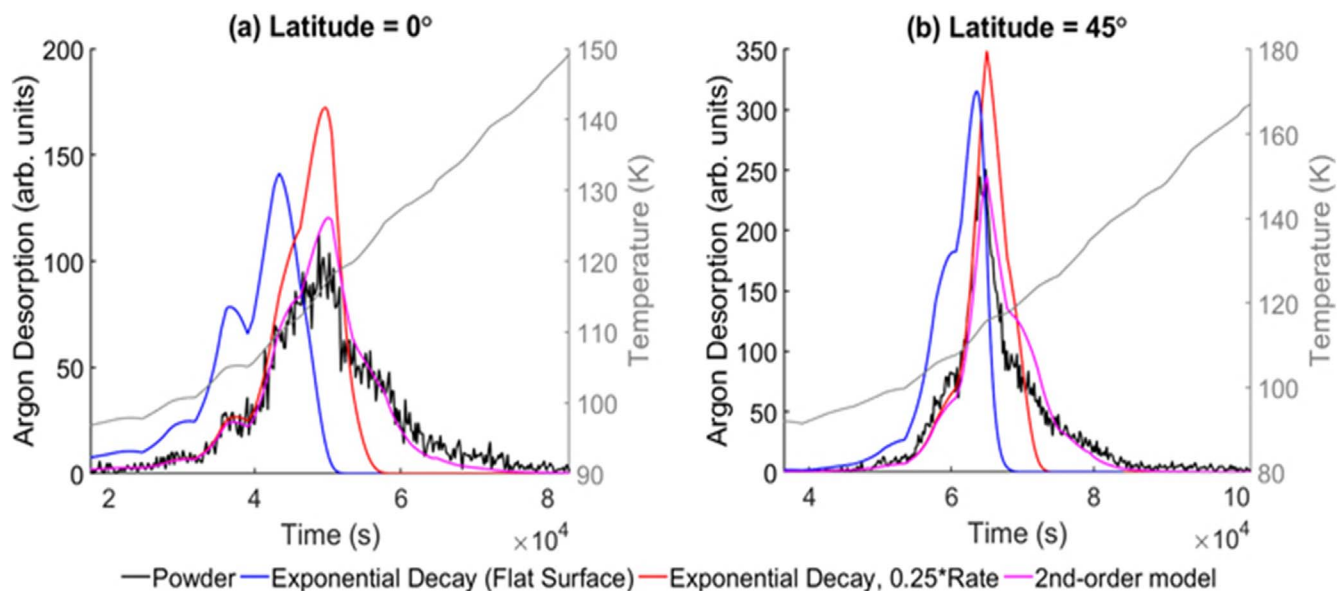
Figure 5. The simulated release of adsorbed argon from a computer-generated powder (in black) at two different latitudes is gradual near the sunrise terminator. In contrast, models that do not account for inward diffusion (blue and red) and that treat desorption as an exponential decay of the adsorbate reservoir underestimate the gas residence time. It does not suffice to simply increase the residence time (contrast blue vs. red curves). Rather, the distribution of waiting times is not exponential; either it can be described as a second-order desorption (magenta line) ,or it can be interpreted as a distribution of adsorption energies. From Sarantos & Tsavachidis (2021).

irradiated soda glass with electrons having energy exceeding ∼20 eV and found the Na^+ and K^+ emission to increase with increasing surface temperature.

4.2. Thermal Accommodation and Subsurface Diffusion

A diurnal cycle of exospheric gas density is driven by planetary rotation. Different gas species exhibit different trends with local time as a result of the different ways in which they interact with the surface. The main parameters influencing the diurnal cycle are the thermal desorption barrier, the accommodation coefficient, and the subsurface diffusion (Kegerreis et al. 2017; Sarantos & Tsavachidis 2021).

The first consideration is whether or not a particular gas adheres to the cold nightside surface. When the interaction potential of deposited particles (adsorbates) with the surface exceeds the random thermal motion at typical nightside temperatures, gases adsorb, and the exosphere diminishes from dusk to dawn. An example of this behavior is demonstrated by lunar argon (e.g., Grava et al. 2015, 2021 and references therein). On the other hand, for species that only temporarily adhere and thermally accommodate with the surface even at the coldest temperatures, flux balance between atoms on the surface and atoms in flight dictates that surface temperature and gas density are roughly related via the relationship $n \sim T^{-5/2}$ (Hodges & Johnson 1968). That is, temperature variations across local times and the corresponding gas residence time variations contribute to lateral transport of gas. This trend is observed for lunar neon (Benna et al. 2015). Lunar helium is an intermediate case, as it is observed to peak at 2 AM because its large scale height does not permit gas to remain localized, as the Hodges & Johnson (1968) flux balance calculation assumed. Helium at the Moon appears to thermally accommodate as a result of multiple energy exchange interactions with the regolith (Hodges 1980; Grava et al. 2021). However, at Mercury, the helium data have been interpreted to indicate

deviations from full thermal accommodation (Leblanc & Chaufray 2011).

Subsurface diffusion contributes to the diurnal trend because it prolongs the gas residence time inside the regolith (Hodges 1982). Kegerreis et al. (2017) noted that the diurnal trend of lunar argon gas could be reconciled with gas adsorption energies as determined experimentally if one also accounts for the possibility of long trapping times in lunar grain voids. To emphasize this point, Sarantos & Tsavachidis (2020, 2021) used trajectory calculations of trace gases in spherical packing that resembled regolith. The increase in residence time of gas prior to exit to vacuum acted as an effective distribution of binding energies and permitted a more gradual release of argon near the sunrise terminator (Figure 5).

An additional complication for Mercury is that its rotation rate with respect to the Sun is nonuniform during a Mercury year, and the micrometeoroid impact rate onto the dawn hemisphere is higher closer to the Sun (Pokorný et al. 2018). This effect leads to a situation where the dayside gas content peaks near aphelion for species that freeze out at night (e.g., Mura et al. 2023). In fact, the micrometeoroid impacts maximize at the same longitudes of the warm poles. Furthermore, seasonality for exospheric species like sodium, magnesium, and calcium is driven by the fact that their surface source rate varies periodically over a Mercury year (e.g., Leblanc & Johnson 2003; Mura et al. 2009; Pokorný et al. 2018; Merkel et al. 2017; Moroni et al. 2023).

4.3. Exospheric Features Related to Warm Longitudes

In Cassidy et al. (2016), a persistent peak in the equatorial sodium exosphere of Mercury over one orbit of Mercury (Figure 6) was highlighted from the observations by the MESSENGER Mercury Atmospheric and Surface Composition Spectrometer (MASCS) instrument in relation to the warm longitudes (blue lines in Figure 1). In their paper, the authors suggested that the origin of this feature was a combination of
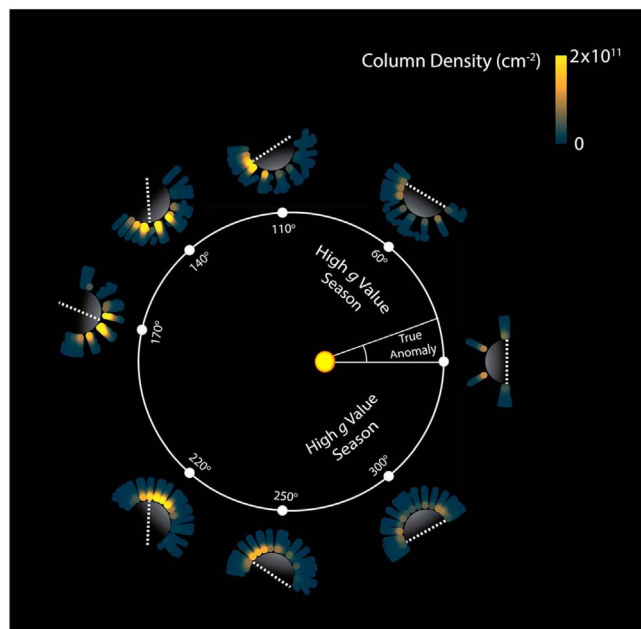
Figure 6. Observed sodium limb column density (with line-of-sight tangent points below 30° in latitude) projected onto Mercury's equatorial plane over the course of a Mercury year. The white dashed lines indicate the position of the warm longitudes as Mercury rotates. From Cassidy et al. (2016).

Figure 7. The effects of target temperature on the production rates for impact melt and vapor. The Hermean flux assuming a circular orbit for the planet at 0.387 au is used for illustrative purposes. From Cintala (1992).

absorption favored by an on-average colder surface combined with the solar pressure inducing a peak in the day-to-nightside migration during the perihelion portion of Mercury's orbit. Both effects would contribute to enhancing the trapping of exospheric sodium atoms in the surface at the warm longitudes that would be gradually released over subsequent portions of Mercury's orbit.

Leblanc et al. (2022) simulated these processes with a three-dimensional time-dependent exospheric model (Mura et al. 2009; Leblanc & Johnson 2010) but concluded that the main persistent feature of Mercury's sodium exosphere should be a dawn enhancement due to Mercury's diurnal rotation and a permanent day-to-nightside cycle; however, they were not able to reproduce the MESSENGER observations. These authors concluded that the origins of these observations should be driven on geological timescales by the difference in heat received by the warm longitudes with respect to the rest of the planet (Figure 2). Such a difference would lead to long-term thermal surface weathering (Section 5.1) of the warm longitude surface by modifying the efficiency to trap and release the sodium exospheric atoms at this particular longitude with respect to the rest of the surface. Put another way, the warm longitude surface has to be the main reservoir of sodium for Mercury's exosphere, the rest of the surface being significantly depleted in sodium.

5. The Role of Temperature in Space Weathering

The "classical" space-weathering processes are bombardment of the surface by micrometeoroids and solar wind irradiation. Both processes work to amorphize the rims of regolith grains and produce submicroscopic iron particles (e.g., Hapke 2001). Here we examine how temperature affects these processes and induces others that alter the structure and chemistry of Mercury's surface and how these ultimately affect the composition and spectral properties.
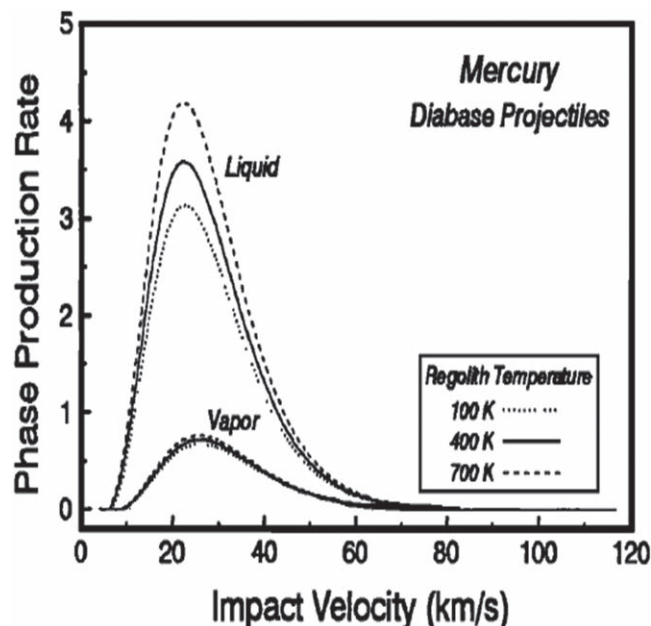
5.1. Temperature and Weathering Effects

Examination of the spectral observations acquired by MESSENGER's MASCS Visible and Infrared Spectrograph show no definitively diagnostic mineral features (e.g., Izenberg et al. 2014; Murchie et al. 2018). Mineralogy has been inferred from elemental chemistry observations from MESSENGER's X-Ray Spectrometer and its Gamma-Ray and Neutron Spectrometer (GRNS). Vander Kaaden et al. (2017) showed that the calculated silicate mineralogy is dominated by plagioclase, pyroxene, and olivine and that the rocks on the surface vary from komatiitic to boninitic. While the surface temperatures on Mercury vary from ∼100 to ∼700 K (e.g., Morrison 1970; Chase et al. 1976; Paige et al. 2013; Bauch et al. 2021), they are well below the solidus temperatures for komatiites (Faure et al. 2006) or boninites (e.g., Duncan & Green 1987). Thus, we do not expect melt or flow from these derived rock mineralogies. However, we do expect these temperatures to affect the surface, since they partially control processes such as micrometeoroid impact and solar wind irradiation and drive thermomechanical weathering (each discussed below).

Cintala (1992) examined the differences in impact velocity, impactor flux, and surface temperature between the Moon and Mercury in the production of impact melt and vapor. Comparing the minimum temperature of both the lunar and Mercury surface of 100 K and Mercury's maximum surface temperature of 700 K, approximately 30% more melt and 15% more vapor is produced at Mercury's maximum temperature. Figure 7 shows how the liquid melt and vapor production varies over Mercury's temperature range. This difference in melt and vapor production due to temperature is secondary to the differences produced by impact velocity and impactor flux. Cintala (1992) estimates that the flux at Mercury is ∼5.5 greater than at the Moon, with a 60% greater mean impact velocity. These three effects (impact velocity, impactor flux, and surface temperature) combine to create a rate of impact melt generation per unit area 13.5 times greater on Mercury

than the Moon, with a factor of 19.5 more vapor production. The vapor generation on Mercury is approximately a factor of 2.9 more than the melt production on the lunar surface. This is important for understanding the surface's glass and agglutinate content.

The lunar soil samples show that agglutinates constitute ∼50% of the particles in sieve fractions <0.5 mm (Heiken 1975; Morris et al. 1983; Hörz & Cintala 1997). They are formed from the glass-welded aggregation of regolith particles, and considering the higher melt and vapor production, they should be a dominant component of Mercury's regolith. Cintala (1992) even argues that little crystalline material is likely to survive in the upper layers of the regolith, and that the continual reworking of the regolith by impact melting and vaporization and solar wind radiation should result in a highly reduced Fe^{2+} content in these glasses. Thus, it is not only pyroclastic deposits that will be rich in glasses, but the entire surface.

Properties of agglutinates from their impact formation include (1) the engulfing of local small grains prior to the melt cooling, which results in the release of solar wind–produced gases from the engulfed grains that can be trapped in the glass as it cools; (2) the release of implanted solar wind material from the melted grains; and (3) the reduction of FeO to form nanometer-sized droplets of metallic phase iron (npFe) that get incorporated into the agglutinate (e.g., McKay et al. 1991; Domingue et al. 2014). The vapor deposition on nearby grains also forms amorphous rims that contain npFe.

Temperature has an effect on the size of npFe particles through the process of Ostwald ripening, where in time the npFe condenses into droplets that grow in size while their number density decreases (e.g., Noble & Pieters 2003; Domingue et al. 2014). In a vapor deposition experiment conducted by Hapke et al. (1994), npFe-rich vapor coatings were heated to a temperature of 924 K for 1 hr. This was sufficient to remove the ferromagnetic resonance (FMR) of the sample. Noble & Pieters (2003) argue that this occurred because the npFe particles had grown to a size larger than the range measurable by FMR techniques, which is 4–33 nm in diameter (Housley et al. 1976). This suggests that the npFe particles more than tripled in size (Noble & Pieters 2003).

Thermomechanical processing is the fracturing and breakdown of material through the stresses created by expansion and contraction caused by diurnal temperature variations. This has been examined in terms of microfracturing created along grain boundaries and contacts (Molaro et al. 2015) and for the breakdown of boulders (e.g., Molaro et al. 2017) and applied for either lunar or asteroid conditions (Molaro et al. 2015, 2017, 2020; Tatsumi et al. 2021). In the case of Mercury, the temperature changes cover a much larger range, but the diurnal timescales are also much larger due to the 3:2 spin–orbit resonance.

In examining microfracturing along grain boundaries for the lunar case, Molaro et al. (2015) modeled grain-scale thermoelastic stresses using finite element analysis of microstructures (Langer et al. 2001). They examined mock structures of pyroxene and plagioclase over varying relative abundances over the lunar diurnal conditions applicable to extensive exposed rock faces (rock exposures, such as bedrock or cliffs) rather than boulders (meter-scale, disaggregated material). Molaro et al. (2015) found that it is not only the temperature but also the heterogeneity of the material that
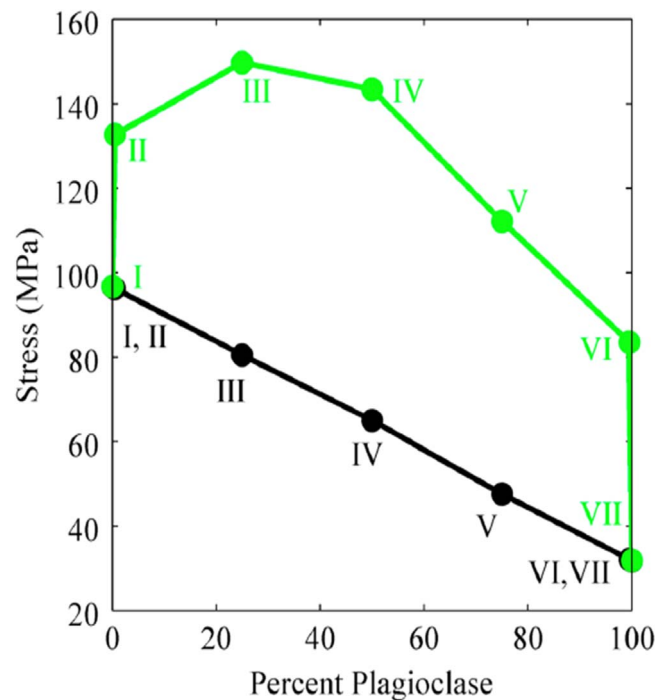

Figure 8. The average (black) and maximum (green) stresses induced during the state of peak tension in a microstructure with a given percentage of pyroxene and plagioclase grains. The values of each point on the plot are given in Table 1. From Molaro et al. (2015).

Table 1
The Percentage of Pyroxene and Plagioclase Present in Microstructures I–VII, as well as the Average and Maximum Stresses Induced in Each during the State of Peak Tension

Microstructure	%Pyroxene	%Plagioclase	Peak Average (MPa)	Peak Maximum (MPa)
I	100	0	97	97
II	99.995	0.005	96	133
III	75	25	73	150
IV	50	50	65	143
V	25	75	47	112
VI	0.005	99.995	32	84
VII	0	100	32	32

controls the thermoelastic behavior (Figure 8, Table 1). The role of compositional heterogeneity is also evident in the range of stresses experienced over the lunar day (Figure 9, left) and the average versus peak stresses (Figure 9, right) experienced over the diurnal cycle. These stresses can cause disaggregation of rock faces and the breakdown of exposed bedrock and rock outcrops, another mechanism for forming regolith.

Molaro et al. (2017) examined thermally induced stresses in boulders for the lunar case and their role in breaking down these larger surface materials. The location of the stresses induced (interior versus surface) is a function of time of day. Stresses occur in boulder interiors at sunrise due to the large-scale temperature gradients developed by overnight cooling, whereas at sunset, the stresses occur at the boulder exteriors due to the cooling and contraction of the surface. The magnitude of the stresses is also dependent on the boulder size. Boulders of 1 m diameter experience peak stresses on the order of 10 MPa (large enough to drive crack propagation in
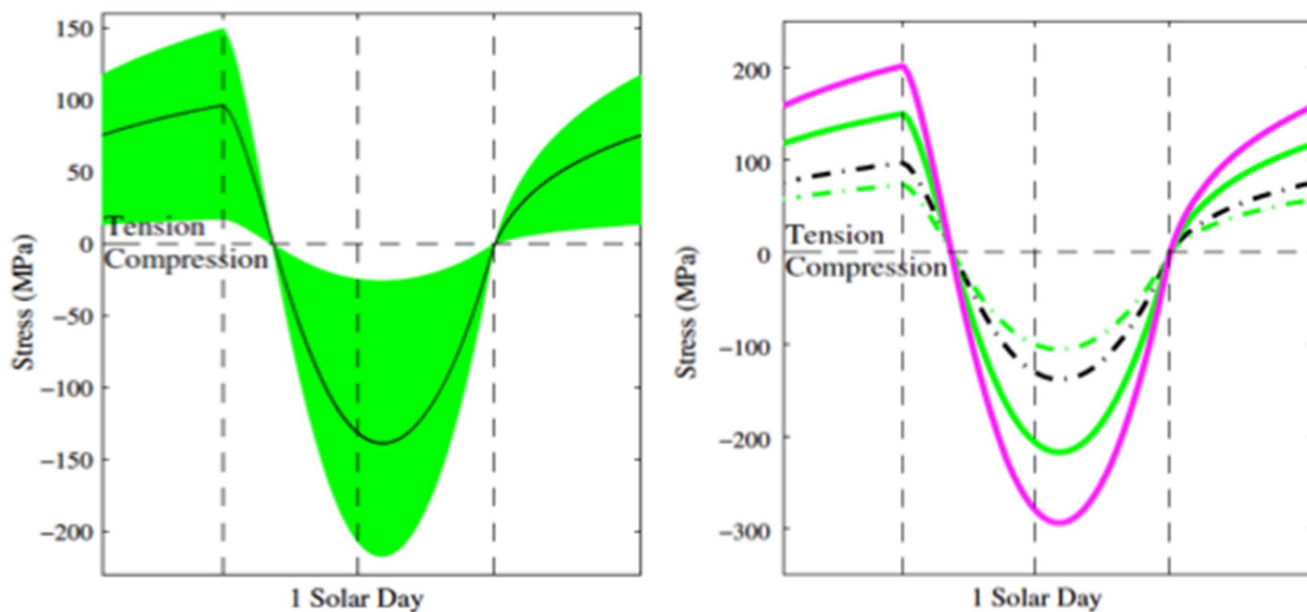
Figure 9. (Left) Profile of the range of stresses experienced within a microstructure over one lunar diurnal cycle for a flat equatorial lunar surface. A homogeneous pyroxene microstructure (black line) is compared to a standard structure of 75% pyroxene and 25% plagioclase grains (green envelope). (Right) Profiles of average (dashed lines) and peak (solid lines) stresses over one lunar diurnal cycle for a homogeneous pyroxene microstructure (black), a standard microstructure (green), and a standard microstructure including cracks (magenta). In both panels, the vertical dashed lines represent sunrise, noon, and sunset, from left to right. Tensile stresses are represented as positive values, and compressional stresses are represented as negative values. From Molaro et al. (2015).

terrestrial environments); however, the stresses decrease as boulder size/diameter decreases, implying that larger boulders break down more rapidly. In larger boulders (>1 m), the thermal wave loses contact with the boulder interior, limiting stresses to the near-surface and confining stresses to the diurnal skin depth. Boulders ⩽30 cm show weak responses to thermal forcing, implying that there is a threshold in size below which crack propagation may not occur; thus, this is not a regolith grain phenomenon. Comparisons of the internal and surface stresses as a function of boulder size over a lunar diurnal cycle are shown in Figure 10. Molaro et al. (2017) found that rocks/ boulders shielded by even a thin layer of regolith are isolated from significant thermal stresses. Therefore, boulders developing partial regolith cover via disaggregation and granular disintegration of their surfaces may eventually shield themselves from further breakdown via thermal processing.

5.2. Temperature-dependent Spectral Signatures

The spectral reflectance behavior from the ultraviolet (UV) to the mid-IR is governed by composition, physical structure, and temperature. It is important to note, as discussed above, that there are both compositional and physical changes that are correlated to temperature, and these will affect the spectral properties as much as the temperature of the material.

Both micrometeoroid and solar wind bombardment produce amorphous materials with embedded npFe particles. Laboratory experiments mimicking these processes suggest that they operate on very different timescales (Hapke 2001; Sasaki et al. 2001; Strazulla et al. 2005), where solar wind bombardment operates at a rate ∼2 orders of magnitude faster than micrometeoroid bombardment at 1 au (Loeffler et al. 2009). Vernezza et al. (2009) provide estimates that micrometeorite bombardment will fully mature (maturate) in 10^8–10^9 yr, whereas solar irradiation will maturate a surface in 10^4–10^6 yr. These timescales indicate the time needed to process the

surface such that the material within the regolith has been fully weathered. These process-dependent timescales are supported by the scales identified in the lunar soil sample studies (Keller & Zhang 2015; Pieters & Noble 2016). Solar flare track densities examined in mature lunar soil samples indicate that the space-weathered rims from both processes accumulate in ∼ 10^6–10^7 yr, suggesting that neither process dominates on the lunar surface (Keller & Zhang 2015; Pieters & Noble 2016). It is highly plausible that even with the solar wind shielding of the surface by Mercury's magnetic field, micrometeoroid bombardment has fully matured the regolith.

As discussed earlier, the size of the npFe weathering products will be a function of temperature, and it is not only their abundance but also their size that governs their alteration of spectral signatures. These npFe particles can be categorized into two size fractions, each affecting the spectral properties differently. The nanoscale (<40 nm) size fraction decreases reflectance and absorption band depths and creates a steeper, redder spectral slope in the visible to near-IR (Vis-NIR; Noble et al. 2007) and a bluer spectral slope in the UV to visible (UV-Vis; e.g., Hendrix et al. 2016). The microscale (>40 nm) size fraction uniformly darkens, or decreases, the reflectance and band depths in the Vis-NIR but has no effect on the spectral slope in the Vis-NIR wavelength range (Noble et al. 2007) and similarly darkens but does not strongly affect the UV-Vis slope (Blewett et al. 2021). The examination of anorthite within the lunar soil samples suggests that the production of nanoscale iron is dominated by micrometeorite impacts (Keller & Zhang 2015; Trang & Lucey 2019). The npFe particle sizes seen in the lunar soil samples show that they are >10 nm in agglutinates compared to <5 nm in nonagglutinitic lunar grains (Keller et al. 1998; Denevi et al. 2014), but Noble & Pieters (2003) suggest that the temperatures on Mercury could triple the size of these npFe inclusions, making estimates for npFe particulate sizes of <15 nm within nonagglutinitic rims and >30 nm within agglutinates. This admixture would darken the surface, subdue
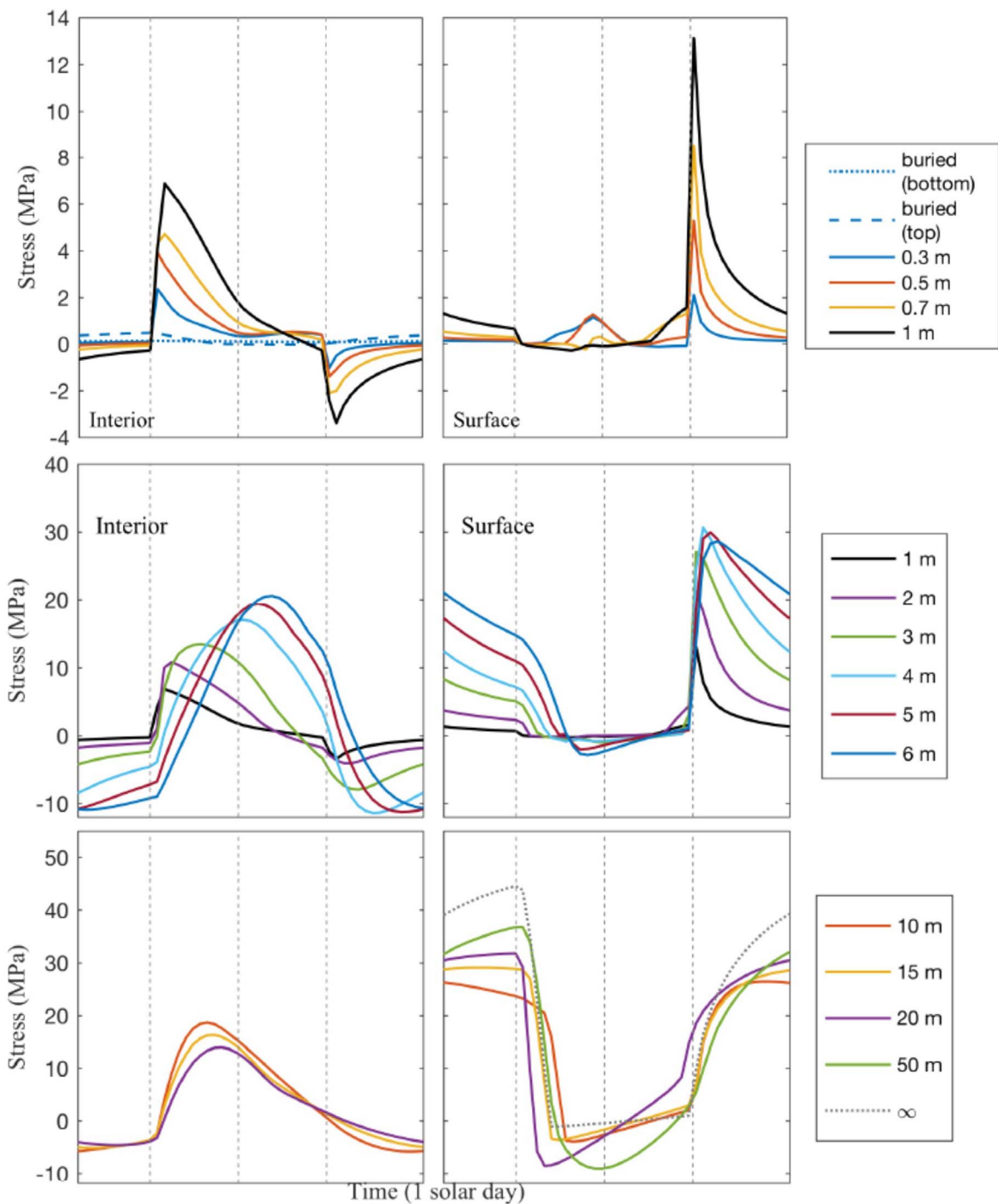
Figure 10. Profiles of the interior (left) and exterior/surface (right) stresses in lunar boulders throughout the lunar day, taken at the location in the boulder where the maximum stress occurs. This is shown for 0.3–1 m (top), 1–6 m (middle), and 10–50 m (bottom) boulders. Dashed lines show sunrise, noon, and sunset from left to right. From Molaro et al. (2017).

absorption features, and create spectral slopes that could potentially correlate with different temperature regimes, assuming uniform FeO content across the surface.

Space weathering, however, is not the only mechanism that can darken, reduce band contrasts, and change spectral slopes in the Vis-NIR. Maturilli et al. (2014) examined temperature effects on the visible and mid-IR properties of komatiites over a range of different iron content and particle size fractions. All of their samples displayed spectral slope changes (reddening) with heating, and many also displayed darkening across both

wavelength regions. The darkening and reddening after thermal processing were independent of ferrous iron content (Maturilli et al. 2014). While their samples displayed spectral changes over both wavelength regions, the X-ray diffraction measurements of their samples confirmed that there were no substantial changes in the primary and secondary mineral phases and no sign of significant oxidation. They attribute the spectral changes to the destruction of color centers, where the samples receive sufficient thermal energy to anneal structural defects, thus destroying color centers. Their heating experiments did

Table 2
Plausible Mineral Analogs for Mercury's Surface Minerals

Silicate Group	Mineral	Chemical Composition	Mineralogy	FeO wt%
Olivine	Forsterite	$Mg_{1.76}Fe_{0.22}X_{0.02}SiO_4$	Fo_{88}	11.06
Pyroxene	Diopside	$(Ca_1Mg_{0.9}Fe_{0.1})Si_2O_6$	$Wo_{50}En_{45}Fs_5$	2.73
	Hypersthene	$(Mg_{1.4}Fe_{0.4}Ca_{0.2})_2Si_2O_6$	$Wo_{10}En_{70}Fs_{20}$	17.84
	Enstatite	$(Ca_{0.01}Mg_{1.73}Fe_{0.25}X_{0.01})Si_2O_6$	$Wo_{0.5}En_{86.5}Fs_{12.5}X_{0.5}$	9.13
Plagioclase feldspars	Anorthite	$Ca_{0.95}Fe_{0.02}Al_{1.9}Si_{2.1}O8$	$An_{95.5}Ab_{4.5}$	0.48
	Labradorite	$Ca_{0.5}Na_{0.3}Al_{1.5}Si_{2.5}O_8$	$An_{51.2}Ab_{46.5}Or_{2.3}$	0.09
	Andesine	$Ca_{0.5}Na_{0.4}Al_{1.5}Si_{2.6}O_8$	$An_{47.4}Ab_{50}Or_{2.6}$	0.35
	Oligolase	$Ca_{0.}Na_{0.6}Al_{1.2}Si_{2.8}O_8$	$An_{19.3}Ab_{76}Or_{4.7}$	0.05
K-feldspar	Microcline	$K_{0.6}Na_{0.4}AlSi_3O_8$	$An_{0.5}Ab_{31.9}Or_{67.6}$	0.04
Feldspathoid	Nepheline	$Na_{0.75}K_{0.18}(Al_{0.95}SiO_4)$	$Neph_{100}$	0.01

not show any appreciable changes in band contrast in the visible.

Measurements by Serventi et al. (2013) show that the mixing of plagioclase of varying FeO content with pyroxene and olivine mineral assemblages increases the overall albedo and reduces the spectral contrast of the mineral assemblages. Increasing the iron content and particle size of the plagioclase in the mixture produces similar effects: a minimum shift toward the IR and an overall decrease of the reflectance (Serventi et al. 2013). Bruschini et al. (2022) demonstrated that graphite mixed with silicate materials also mimics space-weathering spectral trends in the Vis-NIR by reducing albedo and spectral contrast; however, the addition of graphite decreases spectral slopes, in contrast to the space-weathering effects. A 1–5 wt% carbon content in Mercury's average surface has been indicated in the MESSENGER GRNS observations (Peplowski et al. 2015; Klima et al. 2018) and suggested to explain the overall low visible albedo of the surface (e.g., Denevi et al. 2009; Syal et al. 2015). However, these spectral differences have not been examined as a function of temperature.

With only Vis-NIR spectral measurements, such as those from the MESSENGER MASCS instrument, the low spectral contrast, red-sloped spectra have been interpreted to indicate possible plagioclase, high-calcium iron-poor pyroxenes, low-iron orthopyroxene (such as enstatite), and low-iron olivine (such as forsterite; McClintock et al. 2008; Izenberg et al. 2014). But, as has been demonstrated, in this wavelength region, these spectra can be interpreted in a number of ways, especially when temperature effects are factored in. Experiments in the mid-IR in anticipation of the surface mapping by the BepiColombo MERTIS instrument show the potential for this wavelength region to be more diagnostic but not without its caveats.

For example, examination of the spectral behavior of the low-iron olivine forsterite as it experiences temperature changes of ∼420 K (similar to Mercury's day/night temperature differences) shows that in the mid-IR, these spectral changes mimic differences in iron content (Helbert et al. 2013a). Helbert et al. (2013a) demonstrated that the mid-IR spectrum of Fo_{92} ($Mg_{1.84}$ $Fe_{0.16}$ SiO_4), after heating, resembles the spectrum of Fo_{71} ($Mg_{1.42}$ $Fe_{0.68}$ SiO_4), a higher iron content olivine. This spectral change is attributed to the unit cell volume or thermal expansion coefficients changing with temperature. Emissivity measurements of labradorite show irreversible changes in spectral behavior.

Varatharajan et al. (2020) examined a suite of plausible Mercury surface minerals (Table 2) and their mid-IR spectral variations with temperature in anticipation of the MERTIS

observations. They examined changes in five key diagnostics: (1) the wavelength position of the Christensen feature (CF); (2) the wavelength position of the first Reststrahlen band (RB1); (3) the emissivity at the RB1 position; (4) the difference between emissivity at the CF and RB1 positions, or RB spectral contrast; and (5) the wavelength position of the transparency feature, or the first minimum in emission longward of all of the Reststrahlen bands. The emissivity spectra show that for all silicates, the RB1 position shifts longward with increasing temperature, while the RB1 emissivity decreases with temperature; variations in the other diagnostics with temperature are more nuanced (Figure 11; see Varatharajan et al. 2020).

The shifts in the CF position with temperature are subtle for many of the minerals (forsterite, diopside, enstatite, andesine, oligolase, and microcline), while some move noticeably to shorter wavelengths (hypersthene and labradorite), and anorthite moves to longer wavelengths (Varatharajan et al. 2020). It is the relative position of the CF band between these minerals as a function of temperature that is also important to note. If the relative positions at 200 K are compared to the relative positions of the CF band at 500 K, it is clear that enstatite and hypersthene change order, and anorthite becomes much closer to enstatite, hypersthene, and nepheline. Temperature will be a factor in distinguishing between the abundances and variability of these minerals across Mercury's surface.

One of the surprises from the elemental chemistry measurements from the MESSENGER mission, in conjunction with the discovery of the unique hollows morphological features (e.g., Blewett et al. 2011, 2013, 2018) and the confirmation of water trapped within the PSRs (e.g., Lawrence et al. 2013; Chabot et al. 2018), is the high abundance of volatiles (e.g., Nittler et al. 2011). There is a suite of sulfides that have been postulated to be present, especially associated with the hollows regions. The spectral behavior of these minerals with temperature has also been examined and found to behave uniquely, with no obvious trends (e.g., Helbert et al. 2013b; Varatharajan et al. 2019). In the mid-IR, CaS shows deepening of the CF feature near 9 μm, whereas MgS shows depletion of this same feature. In the thermal IR, all sulfides show a darkening with heating, regardless of the phase angle at which the measurement was acquired.

5.3. Thermal Compositional Modifications

As previously stated, the composition of Mercury's surface is dominated by plagioclase, pyroxene, and olivine, and the rocks on the surface vary from komatiitic to boninitic (Vander Kaaden et al. 2017), which are stable and will not melt or flow
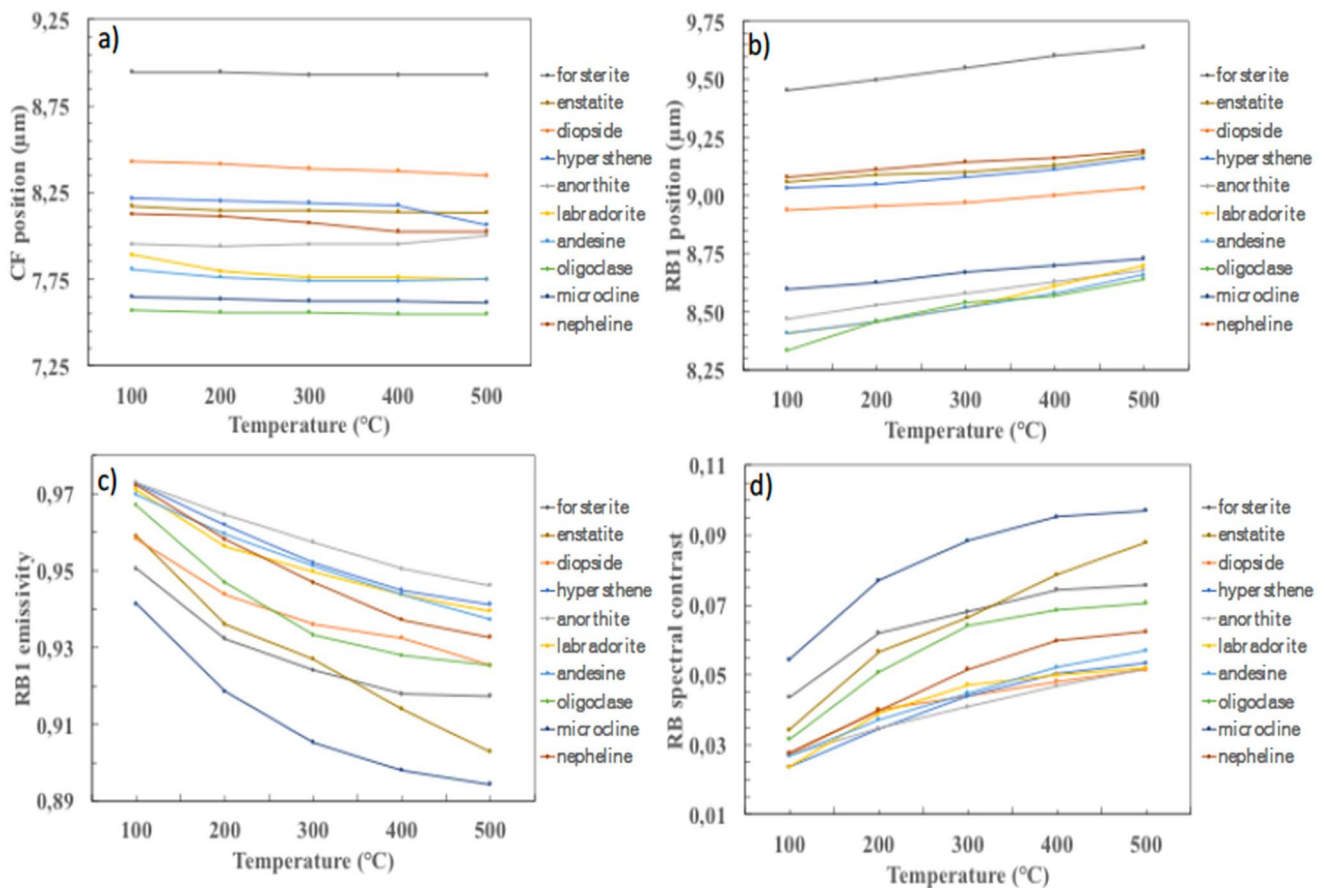
Figure 11. The derived spectral parameters. (a) CF position (μm), (b) RB1 position (μm), (c) RB1 emissivity, and (d) RB spectral contrast (μm) for each silicate are plotted against their corresponding sample temperature. From Varatharajan et al. (2020).

over Mercury's temperature ranges. However, observations from MESSENGER have shown us that there is also a volatile component to the surface composition. Sulfur was detected with an average of ∼4 wt% (Nittler et al. 2011; Evans et al. 2012), compared to the <0.1 wt% in the Earth's typical crust. Other volatile species, such as potassium, thorium, and uranium, are present at average wt% values of ∼1300 ppm, ∼0.16 ppm, and ∼90 ppb (Peplowski et al. 2012; Nittler et al. 2018; Nittler & Weider 2019), respectively. Sodium ranges in value from 2.6 wt% at the equator to ∼5 wt% at high northern latitudes, and chloride varies from 1200 to 2500 ppm from the equator to high northern latitudes (Peplowski et al. 2014; Evans et al. 2015; Nittler & Weider 2019). Hydrogen, which is associated with water in the PSRs, was also detected (Lawrence et al. 2013). These volatiles, their dissociation from H_2O molecules through radiation, and their diffusion through heating, will migrate through the regolith and either be lost to the exosphere or cold trapped within the regolith. The rates of dissociation and diffusion will be affected by the temperature variations across the surface.

The question of the distribution of these volatiles within the surface and how the temperature variations affect their stability becomes an issue. The accumulation of water and potentially other volatiles in the PSRs were discussed in Section 2.2. There are three other morphological units on Mercury that provide insight into the distribution of volatiles within Mercury's crust: hollows, pyroclastic vents, and chaotic terrains.

Hollows are irregularly shaped, flat-floored, shallow depressions that occur predominantly within impact crater

structures (crater floors, walls and rims, central peaks, and ejecta) and are considered very young in age (Blewett et al. 2011, 2013, 2018; Thomas et al. 2014, 2016). They are often, but not always, found in association with low-reflectance materials (Thomas et al. 2014, 2016), a unit considered rich in graphite (Klima et al. 2018). Their morphology suggests that they formed via sublimation of volatiles through a number of mechanisms, including solar heating and heating via contact with magmatic materials or impact melt (Blewett et al. 2011, 2013, 2018; Thomas et al. 2014, 2016; Phillipps et al. 2021). Examination and modeling of the MESSENGER MDIS color imaging and MASCS Vis-NIR observations, coupled with comparisons with laboratory spectral measurements, indicate that the volatile species involved in hollows formation are predominately sulfides, such as CaS, MgS, and NaS (e.g., Barraud et al. 2023), though chlorides have also been considered (e.g., Lucchetti et al. 2021). It has been postulated that these volatiles are either a layer that has been exposed to the surface and subsequently lost either due to sublimation, where sublimation has been halted through the formation of a capping lag deposit (e.g., Blewett et al. 2018), or formed through the interactions of sulfur-rich gases with bedrock (e.g., Phillipps et al. 2021; Renggli et al. 2022).

Pyroclastic volcanism, by its definition, involves the presence and release of volatiles. Examination of the spectral properties of colocated pyroclastic vents and hollows within Tyagaraja crater by Lucchetti et al. (2021) show that the volatile component is compositionally different between the two units, and that the vent deposits are well described by a

combination of sulfides, whereas the hollows may be better represented by a combination of chloride minerals. Comparisons of laboratory spectra of heated sulfides (Helbert et al. 2013b), silicates, chlorides, and graphite with MASCS spectra of various hollows, however, show that sulfides more closely match the spectral properties of hollows (Barraud et al. 2023). In any case, the proposed minerals are comprised of elements that, with the exception of sulfur, have been detected in the exosphere. However, the MESSENGER MASCS instrument was not able to detect sulfur, even if it had been present.

Another unit indicating the presence of a volatile layer within the crust is chaotic terrain. Long thought to have formed from seismic shaking, chaotic terrain may rather have formed via the major, gradual collapse of a volatile-rich layer (based on recent morphological analyses by Rodriguez et al. 2019). The initial removal is associated with the geothermal heating above an intrusive magmatic body with localized, surficial collapse by devolatilization via solar heating (Rodriguez et al. 2019). The composition of this volatile layer is unknown but is hypothesized to be sulfur-, chloride-, and/or potassium-rich (Rodriguez et al. 2019).

The sublimation of a layer of volatiles has implications for their incorporation into the exosphere and their migration across the surface via cold trapping. The hollows and pyroclastic vent regions are highly localized and episodic events, whereas the collapse-forming chaotic terrains are vast and long-lived. The hollows are young (e.g., Blewett et al. 2018), in contrast to the chaotic terrains, which are old (e.g., Rodriguez et al. 2019). Therefore, their introductions of materials to the surface and exosphere are distinct and complex. The potential for cold-trapping these materials via micro cold traps due to surface roughness with their eventual loss or migration to PSRs has not been examined. The volume of material released over different timescales has not been examined.

The depth and global distribution of a volatile-rich layer will affect the thermal gradients within the surface; however, these distributions are unknown. Hollows have an average depth of 24 ± 16 m (Blewett et al. 2011, 2013, 2018), but thermal profiles of the crust with the presence of a layer at this depth have not been evaluated, nor have the implications of heating from below due to magmatic intrusions.

6. The Missing Information

6.1. Evolution of the Surface Spectra

Understanding the surface composition and the processes that modify it is heavily dependent on understanding the spectral properties and what influences their characteristics. It becomes a task in deconvolving the properties that influence spectral response, such as composition, grain size, grain structures (shape, inclusions, crystallinity), and regolith structures (compaction, roughness), with the processes that affect these properties, such as impacts, radiation, and heating. This requires laboratory measurements and theoretical modeling.

There have been many spectral libraries built to construct catalogs as a function of composition; however, the preponderance of these libraries are of minerals acquired under nominal Earth atmospheric conditions. It has been shown that the spectra of minerals relevant to Mercury are different if acquired under inert or vacuum conditions (e.g., Jaramillo et al. 2021, 2022) or

high temperature (e.g., Helbert et al. 2013b; Varatharajan et al. 2019). These studies, however, have been focused on a subset of minerals and a narrow band of wavelengths. A thorough systematic study of end-member minerals at different grain sizes, in vacuum, over 100–700 K temperature variations, and over a broad range of wavelengths (0.2–25 μm) is needed for comparisons to observations and compositional modeling of potential mixtures. This is a large matrix, which has only been partially filled by previous studies.

These spectral libraries form the base for modeling the observed spectra of planetary surfaces. Linear mixing models using such spectral libraries have constrained the composition of hollows volatile materials (Vilas et al. 2016; Varatharajan et al. 2019; Lucchetti et al. 2021). Using intimate mixing models with broad assumptions on the silicate properties of Mercury's surface, the abundances and grain sizes of submicroscopic iron and carbon have been mapped across the surface (e.g., Trang et al. 2017). The abundances are correlated with temperature, implying Ostwald ripening of the submicroscopic iron (Trang et al. 2017). However, the iron content predicted from the model exceeds the measured value from the MESSENGER Gamma Ray Spectrometer (Trang et al. 2017). Intimate mixing modeling, however, requires spectra acquired under environments and conditions representative of Mercury's surface. For example, the change in olivine due to heating mimics an olivine with higher iron content in atmospheric conditions (Helbert et al. 2013b). If such a spectrum is incorporated into a mixing model, this will affect the iron content determinations and may create mismatches between spectral analyses and elemental chemistry observations.

6.2. Diffusion Timescale

The diffusion coefficients of many constituents at radiative doses appropriate to Mercury must be quantified. It has been demonstrated that surface–exosphere reservoir models that do not account for diffusion into regolith consistently underestimate the gas residence time (Sarantos & Tsavachidis 2020, 2021). In computer simulations, common approaches to quantifying gas diffusion between grain voids have relied on generating sphere packings, either of a single size (e.g., Skorov et al. 2011) or with polydisperse distributions (Sarantos & Tsavachidis 2020, 2021). The extraction of diffusion coefficients and free path distributions from such simulations as input to global exosphere–surface interaction models should be pursued as a first step. However, theory and simulation tools that accommodate more realistic particle shapes should be a reasonable next step (Kulchitsky et al. 2018). Notably, it is generally difficult to incorporate a very broad distribution of grain sizes in such simulations; the maximum to minimum grain size was 6 in Kulchitsky et al. (2018) and 12 in Sarantos & Tsavachidis (2021). In previous simulations, the submillimeter size fraction of lunar samples has been used as a proxy of lunar regolith, yet for Mercury, the grain size distribution has not been quantified, except as an estimate of the mean grain size from thermal considerations (Gundlach & Blum 2013).

Diffusion is related to the sticking coefficient and residence time of gas on grains. Here, relevant adsorption–desorption experiments are required on realistic samples and analogs to constrain the distribution of desorption energies for relevant gases and temperatures. Lunar samples may be a good starting point as substrates for such experiments, especially from mature soils (keeping in mind that Mercury's regolith is

probably even more fine-grained than the lunar regolith because of the harsher temperature cycles). In parallel, powders with grain sizes similar to Mercury should be constructed in the laboratory from appropriate analog materials. Furthermore, it is desirable to attempt to experimentally quantify diffusion at the surface of grains (known as surface diffusion). Previous simulations have demonstrated that mobility for photodesorbed species like sodium helps to dislodge adsorbates from microshadows in powders (Sarantos & Tsavachidis 2020). An additional effect of surface mobility is that adsorbates can migrate to chemisorption sites and be trapped, something that will make desorption rates a nonlinear function of temperature (Sarantos & Tsavachidis 2021) and lead to time-dependent diffusion coefficients. A considerable unknown is the activation energy for surface diffusion, which is usually a fraction of the activation energy for desorption.

Besides performing adsorption–desorption experiments, another avenue for determining residence time, adhesion, and surface diffusion barriers is the adoption of molecular dynamics (MD) simulations. MD can be used to track the energy exchange of an incident particle with a surface, and the MD results can provide input into Monte Carlo codes of atom penetration and scattering from regolith. As an example, the interaction between solar wind protons and grains was studied with MD by Leblanc et al. (2023), who quantified the reflection probability as a function of incident energy and direction. These studies must be extended to characterize the interaction of sodium and potassium with relevant Mercury surface analogs. MD on appropriate minerals can also be used to quantify the barrier for surface diffusion.

And, finally, incorporating this input into global surface–exosphere reservoir models will be the last step. This framework will include the diffusion into the subsurface, take into account the thermal gradients of the first few centimeters, and acknowledge the effect of microshadows in reducing the contribution of photodesorption at some local times. At the moment, the only global exosphere model that accounts for diffusion is based on Teolis & Waite (2016) and Teolis et al. (2022), but this model has not been applied to Mercury. Furthermore, next-generation global models must also incorporate the effect of topography on the adopted thermal model using digital elevation models from MESSENGER measurements.[5]

6.3. Characterization of the Dependency of the Ejection Mechanism with Temperature

The energy distribution of the released particles for PSD must be characterized as a function of adsorbate coverage and temperature in laboratory experiments. Yakshinskiy & Madey (2000a, 2004) quantified the PSD speed distribution of sodium from a lunar sample and quartz under high sodium adsorbate coverages (0.22–0.5 of a monolayer). Sarantos et al. (2023) demonstrated that these velocities did not fit the line width measurements of sodium around the Moon; instead, the broader and more energetic distribution proposed by Mura et al. (2009) explained the lunar measurements. Sarantos et al. (2023) attributed the difference between the experiment and the lunar observations to the much lower coverage of adsorbed sodium on the Moon, approaching one-thousandth of a monolayer (Narendranath et al. 2022), and citing laboratory evidence that release at coverages near a monolayer is less energetic than from a "bare" substrate. Thus, PSD speeds need to be

quantified as a function of adsorbate coverage. It is conceivable that surfaces at different latitudes, and thus having different coverages of absorbed sodium, emit adsorbates with different speed distributions. This is contrary to the current assumptions in exosphere models, which attempt to describe the photo-desorption process with a common speed distribution. These experiments need to be conducted at different substrate temperatures to follow up on the suggestion of Gamborino & Wurz (2018) that a temperature dependence of the PSD speed distribution be adopted. Note that the experiments cited by Gamborino & Wurz (2018) as evidence were performed at a limited range of temperatures (100–250 K) and not on the same substrate.

The angular distribution for PSD also needs to be characterized as a function of temperature for gas-substrate systems relevant to Mercury. The width of the polar angle distribution increases for stimulated desorption with increasing surface temperature in some systems (e.g., Kiskinova et al. 1988). This, in turn, would affect the directionality of photodesorption from planetary regolith when the Sun is low on the horizon (Sarantos et al. 2023). These experiments should be conducted both on single crystals or smooth surfaces and on powders to confirm the Sarantos et al. (2023) prediction. Sodium and potassium gas would be Mercury-relevant species with which to conduct such experiments, although the proposed effect would apply to other photosensitive volatiles, such as water.

MESSENGER observations of the sodium exosphere (Cassidy et al. 2015) observed a year-to-year stationary profile of the emission intensity corresponding to a typical temperature around 1200 K, that is, much hotter than Mercury's surface temperature. Such observations contradict the theoretical prediction of a partial or total energetic accommodation of the sodium atoms at the surface (Smyth & Marconi 1995), which would imply the existence of a low-altitude layer in the exosphere of thermalized particles. There are very few laboratory experiments constraining the thermal accommodation of particles impacting a surface, and only for flat surfaces (Hunten et al. 1988). Experiments characterizing the energetic accommodation of volatiles impacting surface analogs of the regolith are therefore greatly needed in order to be able to properly model the fate of the exosphere when interacting with the surface (see also Section 4.2). Another key piece of information for the reconstruction of thermal desorption is its dependency with respect to space weathering. As suggested by Cassidy et al. (2016), observations of a correlation between warm longitudes and the sodium exosphere (Section 4.3), along with long-term radiative bombardment of Mercury's surface, might have a strong impact on the intensity of the sources and sinks of the exosphere. Long-term radiative bombardment might be a driver of the surface properties controlling the absorption/desorption, energetic accommodation, and related thermal desorption of the exospheric particles. Laboratory experiments investigating this dependency are therefore needed to confirm or inform our present understanding of the properties of MESSENGER's exosphere observations. Ultimately, the velocity distribution to be adopted in models of thermal desorption needs to be better specified to account for temperature gradients in the regolith, as the temperature gradient affects the lateral migration and the ballistic range of exospheric gases. Time-of-flight experiments could be performed with powders and for various mineralogical

representative samples to address the potentially large range of physical and chemical absorption of volatiles in regolith (Yakshinskiy & Madey 2000b) and their consequences for the energy distribution of the desorbed particles.

7. Conclusions

With a variation between a minimum of less than 100 K (Chase et al. 1976) on the nightside and maximum dayside temperatures of 700 K (Morrison 1970), the thermal conditions at Mercury are a strong driver of both the exosphere and the surface structure and composition. In this paper, we review these conditions, focusing on their impact on the surface/exosphere interfaces.

Several thermal models for the top of the surface have been published, from one-dimensional heat transport models assuming a radiative equilibrium in the first few hundred μm at the surface (Bauch et al. 2021 and references therein) to models coupling heat transport equations with radiative transfer models (Hale & Hapke 2002). Both approaches predict a diurnal cycle in good agreement with the observations (Morrison 1970; Chase et al. 1976), as well as a more than 100 K dayside aphelion-to-perihelion variability. Mercury's high-latitude craters motivate (Vasavada et al. 1999 and references therein) further works devoted to the modeling of PSRs cold enough to harbor water ice stable on geological timescales (Chabot et al. 2013), originally discovered from Earth (Harmon & Slade 1992; Slade et al. 1992) and characterized in detail by MESSENGER (Paige et al. 2013).

We then discuss which properties of the regolith control the surface and subsurface temperature. According to Bandfield et al. (2019), the thermal properties of the regolith are mostly uniform, excluding some specific geologic units. Topography and small-scale roughness are important when considering volatile trapping and transport (Prem et al. 2018). Below the surface, heat conductivity will depend on the physical characteristics of the regolith controlling the relative importance of radiative versus solid heat conductivity (e.g., grain size, porosity, and particulate properties).

We then describe how surface temperature affects the exosphere. The most straightforward relation is the control of the ejection mechanisms, in particular PSD, which has been shown in the laboratory to be temperature-dependent (Yakshinskiy & Madey 2004), but also thermal desorption and energy accommodation, which should produce a population of exospheric particles energetically close to the surface temperature (Yakshinskiy & Madey 2000b). A second obvious signature, previously observed in the argon and helium exospheres of the Moon (Hodges 1975), is the diurnal cycle of the exosphere, evidenced at Mercury for the sodium atomic species (Leblanc et al. 2022). A more complex relation between surface temperature and exosphere is also suggested by the persistent equatorial sodium peak in the exosphere in relation to the warm longitudes observed by Cassidy et al. (2016). We also highlight the importance of the subsurface diffusion induced by the thermal top layer gradient on the exosphere.

We also discuss the main impacts of the surface temperature by reviewing how it controls the regolith structure and mineralogical composition through several mechanisms, for example, Ostwald ripening (e.g., Domingue et al. 2014) and the thermomechanical fracturing and breakdown of material (Molaro et al. 2017). Surface temperature also affects the spectral reflectance properties of a mineral (Maturilli et al. 2014), making the analysis of remote IR and visible observations more difficult. However, the thermal conditions are also a driver of the regolith composition, potentially controlling the distribution of the volatiles in the upper surface on large scales (Peplowski et al. 2014) and at the origin of several morphological units, such as hollows, pyroclastic vents, and chaotic terrains.

Our ability to accurately describe the processes modifying the surface and exosphere induced by these thermal conditions remains poorly supported by direct observations considering the multiparameter dependencies and the remote observations available so far. Therefore, any progress on our understanding of the surface/exosphere interface will probably depend on dedicated laboratory experiments coupled with sophisticated modeling. Modeling efforts should be focused on implementing more accurate descriptions of the many dependencies between the composition and structure of the regolith and Mercury's thermal and radiative environments, as well as their impact on the formation and evolution of the exosphere. Analyzing the available and future observations of Mercury's surface is crucial and needs to be supported by the development of databases to further the analysis of surface spectra acquired in the UV, IR, and visible ranges (Section 6.1). In the same way, thanks to MESSENGER observations of the exosphere, we now have exospheric observations highlighting the role of diffusion and absorption through the top centimeter of the surface and how these processes are driven by the diurnal thermal profile (see Section 6.2). But our understanding of the mechanisms that control such diffusion will also depend on laboratory experiments dedicated to the characterization of the dependency of the different processes for the release of the volatiles into the exosphere with respect to the thermal conditions in Mercury's regolith (Section 6.3).

As a complement to laboratory experiments, the Moon offers us the opportunity to perform in situ experiments in an environment similar to Mercury's. Experiments on the lunar surface dedicated to the characterization of the upper surface, particularly its content of absorbed materials, has been proposed (PROSPECT; Barber et al. 2017) and should greatly help us to better understand Mercury's regolith and its relationship with the exosphere. Landing experiments on the Moon dedicated to this topic are a unique opportunity to perform direct observations of the surface/exosphere interface to further understand the dependencies on the thermal and radiative conditions of an airless body.

ORCID iDs

F. Leblanc ⓘ https://orcid.org/0000-0002-5548-3519
M. Sarantos ⓘ https://orcid.org/0000-0003-0728-2971
D. Domingue ⓘ https://orcid.org/0000-0002-7594-4634
A. Milillo ⓘ https://orcid.org/0000-0002-0266-2556
D. W. Savin ⓘ https://orcid.org/0000-0002-1111-6610

P. Prem ⓘ https://orcid.org/0000-0001-8369-8587
A. Galli ⓘ https://orcid.org/0000-0003-2425-3793

References

Barber, S. J., Smith, P., Wright, I., et al. 2017, in European Lunar Symp. (ELS), PROSPECTing for Lunar Polar Volatiles: The ProSPA Miniature In-situ Science Laboratory

Bandfield, J., Hayne, P. O., Williams, J.-P., Greenhagen, B. T., & Paige, D. A. 2015, Icar, 248, 357

Bandfield, J., Osterloo, M. M., & Holsclaw, G. M. 2019, LPSC, 50, 2653

Barraud, O., Besse, S., & Doressoundiram, A. 2023, SciA, 9, eadd6452

Bauch, K. E., Hiesinger, H., Greenhagen, B. T., & Helbert, J. 2021, Icar, 354, 114083

Becker, K. J., Robinson, M. S., Becker, T. L., et al. 2016, LPSC, 47, 2959

Benna, M., Mahaffy, P. R., Halekas, J. S., Elphic, R. C., & Delory, G. T. 2015, GeoRL, 42, 3723

Blewett, D. T., Chabot, N. L., Denevi, B. W., et al. 2011, Sci, 333, 1856

Blewett, D. T., Denevi, B. W., Cahill, J. T. S., & Klima, R. L. 2021, Icar, 364, 114472

Blewett, D. T., Ernst, C. M., Murchie, S. L., & Vilas, F. 2018, in Mercury: The View after MESSENGER, ed. S.C. Solomon, L.R. Nittler, & B.J. Anderson (Cambridge: Cambridge Univ. Press), 324

Blewett, D. T., Vaaughan, W. M., Xiao, Z., et al. 2013, JGRE, 118, 1013

Breitbach, G., & Barthels, H. 1980, NucTe, 49, 392

Bruschini, E., Carli, C., Bueller, A.-C., et al. 2022, Icar, 378, 114950

Cassidy, T. A., Merkel, A. W., Burger, M. H., et al. 2015, Icar, 248, 547

Cassidy, T. A., McClintock, W.E., Killen, R.M., et al. 2016, GeoRL, 43, 11,121

Chabot, N. L., Shread, E. E., & Harmon, J. K. 2018, JGRE, 123, 666

Chabot, N. L., Ernst, C.M., Harmon, J.K., et al. 2013, JGRE, 118, 26

Chase, S. C., Miner, E. D., Morrison, D., Much, G., & Neugebauer, G. 1976, Icar, 28, 565

Cintala, M. J. 1992, JGR, 97, 947

Colombo, G., & Shapiro, I. I. 1966, ApJ, 145, 296

Cuzzi, J. N. 1974, ApJ, 189, 577

Davidsson, B. J., & Hosseini, S. 2021, MNRAS, 506, 3421

De Beer, M., Rousseau, P. G., & du Toit, C. G. 2018, NuEnD, 331, 248

Denevi, B. W., Robinson, M. S., Boyd, A. K., et al. 2014, JGRE, 119, 976

Denevi, B. W., Robinson, M. S., Solomon, S. C., et al. 2009, Sci, 324, 613

Deutsch, A. N., Chabot, N. L., Mazarico, E., et al. 2016, Icar, 280, 158

Domingue, D. L., Chapman, C.R., Killen, R.M., et al. 2014, SSRv, 181, 121

Duncan, R. A., & Green, D. H. 1987, CoMP, 96, 326

Ernst, C. M., Chabot, N. L., & Barnouin, O. S. 2018, JGRE, 123, 2628

Evans, L. G., Peplowski, P.N., Rhodes, E.A., et al. 2012, JGRE, 117, E00L07

Evans, L. G., Peplowski, P.N., McCubbin, F.M., et al. 2015, Icar, 257, 417

Faure, F., Arndt, N., & Libourel, G. 2006, JPet, 47, 1591

Gamborino, D., & Wurz, P. 2018, P&SS, 159, 97

Glantzberg, A. K., Chabot, N. L., Barker, M. K., et al. 2023, PSJ, 4, 107

Gläser, P., & Oberst, J. 2023, Icar, 391, 115349

Grava, C., Chaufray, J.-Y., Retherford, K. D., et al. 2015, Icar, 255, 135

Grava, C., Hurley, D. M., Feldman, P. D., et al. 2021, MNRAS, 501, 4438

Grava, C., Killen, R., Benna, M., et al. 2021, SSRv, 217, 61

Gundlach, B., & Blum, J. 2012, Icar, 219, 618

Gundlach, B., & Blum, J. 2013, Icar, 223, 479

Hale, A. S., & Hapke, B. 2002, Icar, 156, 318

Hapke, B. 1996, JGR, 101, 16,817

Hapke, B. 2001, JGR, 106, 10,039

Hapke, B., Cassidy, W., Wells, E., et al. 1994, Sci, 264, 1779

Harmon, J. K., & Slade, M. A. 1992, Sci, 258, 640

Harmon, J. K., Slade, M. A., & Rice, M. S. 2011, Icar, 21, 37

Hawkins, S. E., Boldt, J. D., Darlington, E. H., et al. 2007, SSRv, 131, 247

Hayne, P. O., & Aharonson, O. 2015, JGRE, 120, 1567

Hayne, P. O., Aharonson, O., & Schörghofer, N. 2021, NatAs, 5, 169

Heiken, G. 1975, RvGeo, 13, 567

Helbert, J., Nestola, F., Ferrari, S., et al. 2013a, E&PSL, 371, 252

Helbert, J., Maturilli, A., & D'Amore, M. 2013b, E&PSL, 369, 233

Henderson, B. G., & Jakosky, B. M. 1994, JGRE, 99, 19,063

Henderson, B. G., & Jakosky, B. M. 1997, JGRE, 102, 6567

Hendrix, A. R., Greathouse, T. K., Retherford, K. D., et al. 2016, Icar, 273, 68

Hodges, R. R. 1975, Moon, 14, 139

Hodges, R. R. 1980, JGR, 85, 164

Hodges, R. R. 1982, LPSC, 13, 329

Hodges, R. R., Jr, & Johnson, F. S. 1968, JGR, 73, 7307

Hörz, F., & Cintala, M. 1997, M&PS, 32, 179

Housley, R. M., Cirlin, E. H., Goldberg, I. B., & Crowe, H. 1976, LPSC, 7, 13

Hunten, D. M., Morgan, T. M., & Shemansky, D. M. 1988, Mercury (Tucson, AZ: Univ. Arizona Press), 562

Izenberg, N. R., Klima, R. L., Murchie, S. L., et al. 2014, Icar, 228, 364

Jaramillo, C., Pearson, N., Hendrix, A., et al. 2021, AGUFM, P11A–06

Jaramillo, C., Pearson, N., Hendrix, A., et al. 2022, LPSC, 53, 2378

Jones, B. M., Sarantos, M., & Orlando, T. M. 2020, ApJL, 891, L43

Kegerreis, J. A., Eke, V. R., Massey, R. J., et al. 2017, JGRE, 122, 2163

Keller, L. P., Wentworth, S. J., & McKay, D. S. 1998, Workshop on New Views of the Moon: Integrated Remotely Sensed, Geophysical, and Sample Datasets, 44

Keller, L. P., & Zhang, S. 2015, in Space Weathering of Airless Bodies: An Integration of Remote Sensing Data, Laboratory Experiments and Sample Analysis Workshop (Houston, TX: LPI), 2056

Killen, R. M., Sarantos, M., Potter, A. E., & Reiff, P. 2004, Icar, 17, 1

Kiskinova, M., Szabo, A., Lanzillotto, A. M., & Yates, J. T., Jr 1988, SurSc, 202, L559

Klima, R. L., Denevi, B. W., Ernst, C. M., Murchie, S. L., & Peplowski, P. N. 2018, GeoRL, 45, 2945

Krueger, H., Keller, L., Sasaki, S., et al. 2023, PSJ, submitted

Kulchitsky, A. V., Hurley, D. M., Johnson, J. B., Duvoy, P. X., & Zimmerman, M. 2018, JGRE, 123, 972

Langer, A., Fuller, E. R., Jr, & Craig, W. 2001, CSE, 3, 15

Langevin, Y. 1997, P&SS, 45, 31

Lawrence, D. J., Feldman, W.C., Goldsten, J.O., et al. 2013, Sci, 339, 292

Leblanc, F., & Chaufray, J. Y. 2011, Icar, 216, 551

Leblanc, F., Deborde, R., Tramontina, D., et al. 2023, P&SS, 229, 105660

Leblanc, F., & Johnson, R. E. 2003, Icar, 164, 261

Leblanc, F., & Johnson, R. E. 2010, Icar, 209, 280

Leblanc, F., Schmidt, C., Mangano, V., et al. 2022, SSRv, 218, 2

Ledlow, M. J., Burns, J. O., Gisler, G. R., et al. 1992, ApJ, 384, 640

Loeffler, M. J., Dukes, C. A., & Baragiola, R. A. 2009, JGRE, 114, E03003

Lucchetti, A., Pajola, M., Poggiali, G., et al. 2021, Icar, 370, 114694

Maturilli, A., Helbert, J., & St. John, J. M. 2014, E&PSL, 398, 58

McClintock, W. E., Vervack, R. J., Jr, Todd Bradley, E., et al. 2008, Sci, 321, 92

McKay, D. S., Heiken, G., Basu, A., et al. 1991, in Lunar Sourcebook, A User's Guide to the Moon, ed. G. H. Heiken, D. T. Vaniman, & B. M. French (Cambridge: Cambridge Univ. Press), 285

McLain, J. L., Sprague, A. L., Grieves, G. A., et al. 2011, JGRE, 116, E03007

Merkel, A. W., Cassidy, T. A., Vervack, R. J., Jr, et al. 2017, Icar, 281, 46

Mililllo, A., Sarantos, M., Grava, C., et al. 2023, SSRv, 219, 49

Mitchell, D. L., & De Pater, I. 1994, Icar, 110, 2

Molaro, J. L., Byrne, S., & Langer, S. A. 2015, JGRE, 120, 255

Molaro, J. L., Byrne, S., & Le, J.-L. 2017, Icar, 294, 247

Molaro, J. L., Walsh, K. J., Jawin, E. R., et al. 2020, NatCo, 11, 2913

Morgan, T. H., & Shemansky, D. E. 1991, JGR, 96, 1351

Moroni, M., Mura, A., Milill, A., et al. 2023, Icar, 401, 115616

Morris, R. V., Score, R., Dardano, C., & Heiken, G. 1983, Handbook of Lunar Soils, Planetary Materials Branch Pub.67 (Houston, TX: NASA Johnson Space Center) https://curator.jsc.nasa.gov/lunar/catalogs/other/lunar_soils_catalog.pdf

Morrison, D. 1970, SSRv, 11, 271

Mura, A., Plainaki, C., Milillo, A., et al. 2023, Icar, 394, 115441

Mura, A., Wurz, P., Lichtenegger, H. I. M., et al. 2009, Icar, 200, 1

Murchie, S. M., Klima, R. L., Izenberg, N. R., et al. 2018, in Mercury: The View after MESSENGER, ed. S.C. Solomon, L.R. Nittler, & B.J. Anderson (Cambridge: Cambridge Univ. Press), 191

Narendranath, S., Pillai, N. S., Tadepalli, S. P., et al. 2022, ApJL, 937, L23

Neumann, G. A., Cavanaugh, J. F., Sun, X., et al. 2013, Sci, 339, 296

Nittler, L. R., Chabot, N. L., Grove, T. L., & Peplowski, P. N. 2018, in Mercury: The View after MESSENGER, ed. J. C. Solomon, L. R. Nittler, & B. J. Anderson (Cambridge: Cambridge Univ. Press), 30

Nittler, L. R., Starr, R. D., & Weider, S. Z. 2011, Sci, 333, 1847

Nittler, Lr. R., & Weider, S. Z. 2019, Eleme, 15, 33

Noble, S., Pieters, C. M., & Keller, L. P. 2007, Icar, 192, 629

Noble, S. K., & Pieters, C. M. 2003, SoSyR, 37, 31, (Trans. from Astronomicheskii Vestnik)

Paige, D. A., Siegler, M. A., Harmon, J. K., et al. 2013, Sci, 339, 300

Paige, D. A., Wood, S. E., & Vasavada, A. R. 1992, Sci, 258, 643

Peplowski, P. N., Lawrence, D. J., Feldman, W. C., et al. 2015, Icar, 253, 346

Peplowski, P. N., Lawrence, D. J., Rhodes, E. A., et al. 2012, JGRE, 117, E00L04

Peplowski, P. N., Evans, L. G., Stockstill-Cahill, K. R., et al. 2014, Icar, 228, 86

Phillipps, M. S., Moersch, J. E., Viviano, C. E., & Emery, J. P. 2021, Icar, 359, 114306

Pieters, C. M., & Noble, S. K. 2016, JGRE, 121, 1865
Pokorný, P., Sarantos, M., & Janches, D. 2018, ApJ, 86, 31
Prem, P., et al. 2018, Icar, 299, 31
Raines, J., Dukes, C., Milillo, A., et al. 2023, PSJ, submitted
Reiss, P. 2018, Icar, 306, 1
Renggli, C. J., Klemme, S., Morlok, A., et al. 2022, E&PSL, 593, 117647
Rivera-Valentín, E. G., Meyer, H. M., Taylor, P. A., et al. 2022, PSJ, 3, 62
Rodriguez, J. A. P., Leonard, G. J., Kargetl, J. S., et al. 2019, NatSR, 10, 4737
Rognini, E., Mura, A., Capria, M. T., et al. 2022, P&SS, 212, 105397
Rubanenko, L., Mazarico, E., Neumann, G. A., & Paige, D. A. 2018, JGRE, 123, 2178
Ryan, A. J., Pino Muñoz, D., Bernacki, M., et al. 2022, JGRE, 127, e2022JE007191
Ryan, A. J., Pino Muñoz, D., Bernacki, M., & Delbo, M. 2020, JGRE, 125, e2019JE006100
Sakatani, N., Ogawa, K., & Iijima, Y. 2017, AIPA, 7, 015310
Sarantos, M., & Tsavachidis, S. 2020, GeoRL, 47, e2020GL088930
Sarantos, M., & Tsavachidis, S. 2021, ApJL, 919, L14
Sarantos, M., Tsavachidis, S., Kuruppuaratchi, D., & Mierkiewitz, E. 2023, PSJ, submitted
Sasaki, S., Kurahashi, E., Yamanaka, C., & Nakamura, K. 2001, Natur, 410, 555
Schörghofer, N., Benna, M., Berezhnoy, A. A., et al. 2021, SSRv, 217, 74
Serventi, G., Carli, C., Sgavetti, M., et al. 2013, Icar, 226, 282
Singh, B. P., & Kaviany, M. 1994, IJHMT, 37, 2579
Skorov, Y. V., van Lieshout, R., Blum, J., & Keller, H. U. 2011, Icar, 212, 867
Slade, M. A., Butler, B. J., & Muhleman, D. O. 1992, Sci, 258, 635
Smyth, W. H., & Marconi, M. L. 1995, ApJ, 441, 839
Soter, S., & Ulrichs, J. 1967, Natur, 214, 1315
Sprague, A. L., Hunten, D. M., & Lodders, K. 1995, Icar, 118, 211
Strazulla, G., Dotto, E., Binzel, R., et al. 2005, Icar, 174, 31
Syal, M., Schultz, P., & Riner, M. 2015, NatGeo, 8, 352
Tatsumi, E., Sakatani, N., Riu, L., et al. 2021, NatCo, 12, 5837
Teolis, B., Raut, U., Kammer, J. A., et al. 2022, GeoRL, 49, e2021GL097580
Teolis, B. D., & Waite, J. H. 2016, Icar, 272, 277
Thomas, R., Hynek, B., Rothery, D., & Conway, S. 2016, Icar, 277, 455

Thomas, R. J., Rothery, D. A., Conway, S. J., & Anand, M. 2014, Icar, 229, 221
Trang, D., & Lucey, P. G. 2019, Icar, 321, 307
Trang, D., Lucey, P. G., & Izenberg, N. R. 2017, Icar, 293, 206
van Antwerpen, W., du Toit, C. G., & Rousseau, P. G. 2010, NuEnD, 240, 1803
van Antwerpen, W., Rousseau, P. G., & du Toit, C. G. 2012, NuEnD, 247, 183
Vander Kaaden, K. E., McCubbin, F. M., Nittler, L. R., et al. 2017, Icar, 285, 155
Varatharajan, I., Maturilli, A., Helbert, J., Alemanno, G., & Hiesinger, H. 2019, E&PSL, 520, 127
Varatharajan, I., Stangarone, C., Wilke, F. D. H., et al. 2020, ESS Open Archive, essoar.10504660
Vasavada, A. R., Paige, D. A., & Wood, S. E. 1999, Icar, 141, 179
Vernezza, P., Binzel, R.P., Rossi, A., Fulchignoni, M., Birlan, M., et al. 2009, Natur, 458, 993
Vervack, R. J., Jr, Killen, R. M., McClintock, W. E., et al. 2016, GeoRL, 43, 11,545
Vilas, F., Domingue, D. L., Helbert, J., et al. 2016, GeoRL, 43, 1450
Watson, K. 1964, PhD thesis, Caltech https://thesis.library.caltech.edu/4399/1/Watson_k_1964.pdf
Wechsler, A. E., Glaser, P. E., & Fountain, J. A. 1972, in Thermal Characteristics of the Moon, ed. J. W. Lucas (Cambridge, MA: MIT Press), 215
Wesselink, A. J. 1948, BAN, 10, 351
Winter, D. F., & Saari, J. M. 1969, ApJ, 156, 1135
Wohlfarth, K., Wöhler, C., Hiesinger, H., & Helbert, J. 2023, A&A, 674, A69
Wood, S. 2020, Icar, 352, 113964
Wu, H., Gui, H., Yang, X., Tu, J., & Jiang, S. 2020, Int. J. Therm. Sci., 153, 106334
Wurz, P., Galli, A., Jäggi, N., et al. 2023, PSJ, submitted
Wurz, P., et al. 2022, SSRv, 218, 1
Yakshinskiy, B. V., & Madey, T. E. 2000a, SurSc, 451, 160
Yakshinskiy, B. V., & Madey, T. E. 2000b, SRL, 7, 75
Yakshinskiy, B. V., & Madey, T. E. 2004, Icar, 168, 53
Yan, N., Chassefière, E., Leblanc, F., & Sarkissian, A. 2006, AdSpR, 38, 583